

to appear in ApJ

Evolution of Structure in the Intergalactic Medium and the Nature of the Ly α Forest

HongGuang Bi and Arthur F. Davidsen

Center for Astrophysical Sciences, Department of Physics & Astronomy

The Johns Hopkins University, Baltimore, MD 21218

received: 2 July 1996; accepted: 26 October 1996

ABSTRACT

We have performed a detailed statistical study of the evolution of structure in a photoionized intergalactic medium (IGM) using analytical simulations to extend the calculation into the mildly non-linear density regime found to prevail at $z = 3$. Our work is based on a simple fundamental conjecture: that the probability distribution function of the density of baryonic diffuse matter in the universe is described by a lognormal (LN) random field. The LN distribution has several attractive features and follows plausibly from the assumption of initial linear Gaussian density and velocity fluctuations at arbitrarily early times. Starting with a suitably normalized power spectrum of primordial fluctuations in a universe dominated by cold dark matter (CDM), we compute the behavior of the baryonic matter, which moves slowly toward minima in the dark matter potential on scales larger than the Jeans length. We have computed two models that succeed in matching observations. One is a non-standard CDM model with $\Omega = 1$, $h = 0.5$ and $\Gamma = 0.3$, and the other is a low density flat model with a cosmological constant (LCDM), with $\Omega = 0.4$, $\Omega_\Lambda = 0.6$ and $h = 0.65$. In both models, the variance of the density distribution function grows with time, reaching unity at about $z = 4$, where the simulation yields spectra that closely resemble the Ly α forest absorption seen in the spectra of high z quasars. The calculations also successfully predict the observed properties of the Ly α forest clouds and their evolution from $z = 4$ down to at least $z = 2$, assuming a constant intensity for the metagalactic UV background over this redshift range. *However, in our model the forest is not due to discrete clouds, but rather to fluctuations in a continuous intergalactic medium.* At $z = 3$, typical clouds with measured neutral hydrogen column densities $N_{HI} = 10^{15.3}, 10^{13.5}$, and $10^{11.5}$ cm $^{-2}$ correspond to fluctuations with mean total densities approximately 10, 1, and 0.1 times the universal mean baryon density. Perhaps surprisingly, fluctuations whose amplitudes are less than or equal to the mean density still appear as “clouds” because in our model more than 70% of the volume of the IGM at $z = 3$ is filled with gas at densities below the mean value.

We find that the column density distribution of Ly α forest lines can be fit to $f(N_{HI}) \propto N_{HI}^{-\beta}$, with $\beta = 1.46$ in the range $12.5 < \log N_{HI} < 14.5$, matching recent

Keck results. At somewhat higher column densities the distribution steepens, giving $\beta = 1.80$ over the range $14.0 < \log N_{HI} < 15.5$, and matching earlier observations for these stronger lines. The normalization of the line numbers in our model also agrees with observations if the total baryon density is $\Omega_b = 0.015h^{-2}$ and the ionizing background intensity is $J_{21} = 0.18$. Alternatively, if $J_{21} = 0.5$ as recently estimated for the background due to observed quasars at $z = 2.5$, then $\Omega_b = 0.025h^{-2}$ yields the observed number of Ly α lines and the observed mean opacity. The model predicts that about 80% of the baryons in the universe are associated with Ly α forest features with $13 < \log N_{HI} < 15$ at $z = 3$, while 10% are in more diffuse gas with smaller column densities and 10% are in higher column density clouds and in collapsed structures, such as galaxies and quasars. Our model requires that absorbers at $z = 3$ with column densities higher than about 10^{16} cm^{-2} – Lyman limit systems and damped Ly α systems – represent a separate population that has collapsed out of the IGM.

We find the number density of forest lines is $dN/dz = 75[(1+z)/4]^{2.5}$ for lines with $EW > 0.32\text{\AA}$, also in good agreement with observations. We fit Voigt profiles to our simulated lines and find a distribution of b parameters that matches that obtained from similar fits to real spectra. The effective opacity in the Ly α forest is found from the model to be $\tau_{eff} = 0.26[(1+z)/4]^{3.1}$, again in good agreement with observations. The exponents for the evolution of the number of lines and the effective opacity do not simply differ by 1.0, as in the standard cloud picture, owing to saturation effects for the stronger lines. This also explains why the effective opacity evolves more slowly than $(1+z)^{4.5}$, which is expected for the Gunn-Peterson effect in a uniform medium with $J = \text{constant}$ (and $\Omega = 1$).

We compare the spectral filling factor for our CDM and LCDM models with observations of the Ly α forest in HS 1700+64 and find good agreement. Similar calculations for a standard CDM model and a cold plus hot dark matter model fail to match the observed spectral filling factor function. We have also compared a number of predictions of our analytical model with results of numerical hydrodynamical calculations (Miralda-Escudé et al. 1996) and again find them to be in good agreement. The lognormal hypothesis, coupled with otherwise attractive CDM-dominated cosmological models, appears to provide a plausible and useful description of the distribution of photoionized intergalactic gas and provides a new estimate of the baryonic density of the universe.

Subject headings: intergalactic medium, quasars: absorption lines, cosmology: large-scale structure of the Universe, hydrodynamics, dark matter

1. Introduction

Ever since the discovery of quasars with redshifts sufficiently large to bring the Ly α resonance line of neutral hydrogen into the optical band, the possibility of using this line to probe conditions in the intergalactic medium (IGM) has engendered intense interest. Gunn & Peterson (1965) showed that a diffuse, uniform IGM having the critical density must have been very highly ionized at $z = 2$ to avoid producing a very large HI opacity at wavelengths just below that of the quasar's Ly α emission line. Motivated by the Gunn-Peterson idea, Bahcall & Salpeter (1965) pointed out that the Gunn-Peterson effect could be used to probe the IGM at various redshifts (and for other elements), and also suggested that gas that was not uniformly distributed would produce discrete Ly α absorption lines. They were then thinking specifically of gas clumped into clusters of galaxies, but a small generalization will allow us to refer to any localized Ly α absorption in the IGM as the “Bahcall-Salpeter effect”. The subsequent discovery of large numbers of discrete absorption lines at wavelengths below redshifted Ly α (Lynds 1971) lead to the description of this phenomenon as the “Ly α forest”. Their large numbers showed that these forest lines could not be associated with galaxy clusters, and after a period of uncertainty as to whether the lines might be associated with local material ejected from the quasars at high velocities, the idea took hold that the Ly α lines arise in discrete intergalactic clouds at various cosmological redshifts along the line of sight (Sargent et al. 1980; Weymann, Carswell & Smith 1981; Blades, Turnshek & Norman 1988). Observations at relatively high spectral resolution revealed no continuous absorption between the discrete lines, placing strong limits on the Gunn-Peterson effect, and leading to the idea that the Ly α “clouds” might be confined by the pressure of a diffuse, very hot, intercloud medium. Over time this two phase notion lead to the identification of the *intercloud* medium with the *intergalactic* medium, while the Ly α clouds became a somewhat separate subject of study.

In this paper we wish to resurrect the concept of a unified, though not uniform, intergalactic medium, consisting of all the gas that has not collapsed into systems with densities much more than an order of magnitude above the mean baryon density of the universe. In the model we have developed, relatively small amplitude fluctuations in the density of the IGM can explain numerous aspects previously attributed to the discrete cloud picture. We suggest that the Ly α forest is nothing more than the observable manifestation of the Bahcall-Salpeter effect, which is in turn just a generalization of the Gunn-Peterson effect to the case of a nonuniform intergalactic medium.

Our approach has the merit of great simplicity, with numerous predictions following from a small number of fundamental assumptions. The most important of these assumptions is that the probability distribution function of the density of diffuse matter in the universe is described by a lognormal (LN) random field. The LN distribution has several attractive features and follows plausibly from the assumption of initial linear Gaussian density and velocity fluctuations at arbitrarily early time (Coles & Jones 1991). It has the correct asymptotic behavior on large scales or at very early times where the IGM evolves linearly, and it matches the isothermal hydrostatic solution on very small scales such as that for intracluster gas. We also find it to be roughly correct when compared to the statistics of the density distribution in some recent numerical simulations

(see §2.1).

We further assume that the IGM is photoionized by a metagalactic UV radiation field whose intensity is sufficient at $z = 2 - 4$ to reduce the neutral fraction of hydrogen to less than 10^{-5} for gas at the mean density. With a suitable choice of Ω_b , taken to be the nominal baryon density from standard Big Bang nucleosynthesis, for example, this assumption can be satisfied using the intensity provided by the known quasar population.

Our investigation of the model developed here has been motivated by the recent detection of the HeII Gunn-Peterson/Bahcall-Salpeter effect (Miralda-Escudé & Ostriker 1990; Davidsen 1993; and Miralda-Escudé 1993) with the Hubble Space Telescope (Jakobsen et al. 1994; Tytler et al. 1995) and the Hopkins Ultraviolet Telescope (Davidsen & Fountain 1985; Davidsen 1993; Davidsen, Kriss & Zheng 1996, hereafter DKZ). The HUT observation of HS1700+64 yielded an effective HeII Ly α opacity $\tau_{HeII} = 1.0$ at $z = 2.4$. This opacity is too large to be accounted for using the canonical Ly α cloud picture, and lower column density clouds ($N_{HI} \leq 10^{13} \text{ cm}^{-2}$) and/or diffuse gas are needed to explain more than half of the measured He II opacity toward HS1700+64 (DKZ; Zheng, Davidsen & Kriss 1996). The very low density gas in our model contributes very little to the H I opacity, but because the number ratio between He II ions and H I atoms resulting from photoionization by the UV background is large (i.e. $n(HeII)/n(HI) \simeq 100 - 200$), it contributes very significantly to the He II opacity. In this paper we develop our IGM model and concentrate on comparisons with observations of the HI Ly α forest and with other theoretical work. Application of the model to the HeII observations will be discussed in Davidsen et al. (1996). Some of the ideas employed in our model have previously been discussed by Bi, Börner & Chu (1992), Bi (1993) and references therein.

Ly α clouds were suggested to be confined either by an intercloud medium (pressure confinement, e.g. Sargent et al. 1980), or by dark matter mini-halos (Rees 1986). A very hot baryonic medium would distort the blackbody spectrum of the cosmic microwave background radiation through the Sunyaev-Zel'dovich effect. The recent upper limit of the so-called y -parameter has ruled out any cosmologically distributed component of temperature greater than $10^6 K$ (Wright et al. 1994). Thus, the pressure confinement seems unfavored by the COBE results. In the original mini-halo model, baryons are presumed to reside statically in dark matter potential wells. In our model, we allow baryons to move in or out of the wells, depending on the strength of the well. So the dark matter potential wells are more like magnets that direct the motion of baryons but do not trap them. Removing the confinement requirement will introduce a larger cloud size as observed by Dinshaw et al. (1994) and Bechtold et al. (1994).

Historically, there have been several ideas related to unconfined clouds. Black (1981) and Oort (1981) suggested that the Ly α forest might represent relic primordial fluctuations having a characteristic length scale $0.6 - 1.4 \text{ Mpc}$. By assuming UV photoionization heating, Ostriker & Ikeuchi (1983) calculated the temperature of the IGM to be about $1 - 3 \times 10^4 \text{ K}$, very close to that inferred from the widths of the Ly α lines. Even in the mini halo model, the clouds may act

like transient phenomena because the halos merge frequently at high redshift.

The first non-static cloud model was studied by Bond, Szalay & Silk (1988) who suggested that clouds were in a free expansion phase. McGill (1991) illustrated preliminarily that an IGM with the fluctuation variance $\sigma^2 = 1$ could also produce line-like absorptions in quasar spectra through caustic structures in its peculiar velocity field. Bi, Börner & Chu (1992) and Bi (1993) considered a more physical IGM evolution in the hierarchical clustering model and the cold-dark-matter model. They found that such a median fluctuated IGM contains the correct number of density clumps, which have sizes comparable to the Jeans length, and would produce Ly α absorption lines compatible with what are observed. The velocity caustics are a secondary effect when compared to the density fluctuation. The similarity between two nearby absorption profiles, such as seen in gravitationally-lensed quasar spectra, can be consistently accounted for by coherent clustering in the density too. Therefore they suggested that such an alternative phase of the IGM should have played a role in the Ly α forest as important as the conventional clouds. The reason that the $\sigma = 1$ IGM can produce distinguishable line features is that the absorption profile is an exponential function of the optical depth τ , which in turn is approximately proportional to the square of the baryonic density. Therefore a small enhancement (i.e. an overdensity over the local background) in the IGM would result in a large change in $\exp(-\tau)$ at $\tau \simeq 1$ and then appear as a deep absorption line.

The actual fluctuation picture can be obtained by cosmological N-body and hydrodynamical simulations. Recent simulations by Cen et al. (1994), Zhang, Anninos & Norman (1995), Hernquist et al. (1996), and Miralda-Escudé et al (1996) have solved hydrodynamical equations from first principles and have set up a firm evolutionary picture of the IGM. Although they use different techniques and cosmological models, all the simulations indicate a median fluctuated IGM instead of discrete clouds. For instance, from an analysis of published simulations we found the variance of the IGM density is just about 1 at $z = 3$ in Cen et al. (1994) and Miralda-Escudé et al (1996). The density, temperature and thermal pressure of the medium are continuous fields that cannot be attributed simply to gravitational confinement or pressure confinement. Yet the Ly α forest can be produced naturally.

What are the geometry, ionization degree, thermal state and Ly α absorption properties of absorbers in the IGM ? How do the statistical quantities evolve in redshift ? The present paper will study these questions in detail. Related work can be found in Miralda-Escudé et al. (1996, hereafter MCOR). Because of our analytical approach, our simulation can be performed in 1-D, i.e. along one line of sight. This enables us to have a simulation box size almost arbitrarily large, which is necessary for large-scale fluctuation components, as well as to have a very small grid in the same simulation for revealing fine structures *within* Ly α clouds. Different cosmological models with different choices of free parameters can be computed relatively quickly to check various diagnostics in our IGM simulation.

Flat universe models dominated by cold dark matter, with or without a cosmological constant,

will be considered in this paper. We will discuss the assumption of the lognormal field, and our simulation procedure in Section 2. In Section 3.1, the evolution of the volume filling factor and cumulative mass fraction for different density thresholds will show why the IGM should be regarded as a diffuse and continuous medium. Several statistical properties of Ly α absorbers are discussed in Section 3.2, including characteristic size, mean density and neutral fraction. Velocity and density structures within clouds will be studied in Section 3.3. The evolution of HI opacity, cloud number counts dN/dz , and the HI column density distribution will be discussed and compared to observations in Section 4. In Section 5, we compare simulation samples with a high resolution Keck observation of HS1700+64. They agree surprisingly well with each other, not only in general appearance but also in their b parameters, spectral filling factors and spectral autocorrelation coefficients. We have also made some comparisons to MCOR’s simulation in that section. Section 6 summarizes our conclusions.

2. The Lognormal Density Field : Theories and Structures

2.1. Constructing the IGM model

The density distribution of the IGM is assumed to be a lognormal random field,

$$n(\vec{x}) = n_0 \exp[\delta_0(\vec{x}) - \frac{\langle \delta_0^2 \rangle}{2}], \quad (1)$$

where n_0 is the mean number density and δ_0 is a Gaussian random field derived from the density contrast δ_{DM} of dark matter :

$$\delta_0(\vec{x}) \equiv \frac{1}{4\pi x_b^2} \int \frac{\delta_{DM}(\vec{x}_1)}{|\vec{x} - \vec{x}_1|} e^{-\frac{|\vec{x} - \vec{x}_1|}{x_b}} d\vec{x}_1, \quad \text{or } \delta_0(\vec{k}) \equiv \frac{\delta_{DM}(\vec{k})}{1 + x_b^2 k^2}, \quad (2)$$

in the comoving space or the Fourier space, respectively. The comoving scale x_b is defined by

$$x_b \equiv \frac{1}{H_0} \left(\frac{2\gamma k T_m}{3\mu m_p \Omega (1+z)} \right)^{\frac{1}{2}}, \quad (3)$$

where T_m and μ are the mean temperature and molecular weight of the IGM; Ω is the cosmological density parameter of total mass; and γ is the ratio of specific heats. The scale x_b is 2π times smaller than the standard Jeans length $\lambda_b \equiv v_s(\pi/G\rho_c)^{1/2}$, where v_s is the sound speed in the IGM and ρ_c is the total cosmological mass density (Peebles 1980).

The LN approach was introduced by Coles & Jones (1991) to describe the non-linear evolution of dark matter. Here we apply it to the baryonic matter in the IGM. We first discuss the physical background of the LN approach.

At early epochs $z \gg 1$ or on large scales $x \rightarrow \infty$, fluctuations are small, so we have $\delta(\equiv n/n_0 - 1) \simeq \delta_0$ in Eq. 1. This is just the expected linear evolution of the IGM (Peebles 1974;

Fang et al. 1993). On very small scales, we have $|\vec{x} - \vec{x}_1| \ll x_b$ in Eq. 2; thus Eq. 1 becomes the well-known isothermal hydrostatic solution, which describes highly clumped structures such as intracluster gas,

$$n \propto \exp\left(-\frac{\mu m_p}{\gamma k T} \psi_{DM}\right), \quad (4)$$

where ψ_{DM} is the dark matter potential (Sarazin & Bahcall 1977).

During the linear evolution of dark matter fluctuations, ψ_{DM} is constant, being as small as that at the decoupling time. Therefore, one expects that the potential would remain linear much longer than the density; consequently one can simply use the unchanged primordial potential in the whole calculation. This frozen potential approximation has been tested and found to work well against N-body simulations, and is apparently superior to the Zel'dovich approximation or the frozen-flow approximation (Brainerd, Scherrer & Villumsen 1983; Bagla & Padmanabhan 1994). As long as the dark matter potential is fixed, baryons will move toward the minima in the potential, which are 2-dimensional pancakes. If the evolution is long enough, the final configuration will be the isothermal hydrostatic solution.

In the LN distribution, the 3-D configuration of the IGM is uniquely determined by the primordial distribution. This can be compared to a recent non-linear clustering model, the peak patch theory (Bond, Kofman & Pogosyan 1996). N-body simulations indicated that the final non-linear density field can be fairly reconstructed from individual “peak patches” existing in the original distribution. The LN approach can be viewed alternatively as a very simplified representation of the theory, in which all small scale collisions between nearby particles are neglected.

Among all smooth functions that can link the known linear solution and the hydrostatic solution asymptotically, the LN function is the simplest one. Furthermore, it always defines a positive IGM density. In contrast, any smooth polynomial function of δ_0 will output negative density n when $\delta_0 \rightarrow -\infty$. Because δ_0 is identified as the density contrast in the linear evolution, Eq. 1 transforms the extrapolated linear density to the nonlinear counterpart.

Our conjecture can be tested by comparisons with hydrodynamical simulations. We have made a statistical histogram of $\log \frac{n}{n_0}$ at $z = 3$ in MCOR’s Fig. 7, which turns out to be fitted well by a Gaussian probability function with variance $\sigma^2 = 1.0$ and the mean -0.52. Note that according to Eq. 1, the mean should be equal to $-\frac{1}{2}\sigma^2$. Based on the same cosmological model, our analytical calculation leads to $\sigma = 1.25$, which is only slightly greater. We found that the results discussed later in the paper are not altered substantially if the smaller variance is adopted. Hence, we suggest that the LN model is a simple, yet acceptable model for the density distribution of the IGM.

A Gaussian random field is uniquely determined by its power spectrum. We will use the cold-dark-matter power spectrum in our simulation of δ_0 . This is (Efstathiou, Bond & White

1992)

$$P(k) \propto k / (1 + (6.4 \frac{k}{\Gamma} + (3.0 \frac{k}{\Gamma})^{1.5} + (1.7 \frac{k}{\Gamma})^2)^{1.13})^{\frac{2}{1.13}}, \quad (5)$$

where $\Gamma = \Omega h$, and h is the normalized Hubble parameter. The amplitude of the spectrum can be normalized by the COBE rms quadrupole $Q_{rms} = 18 \mu\text{K}$. If normalized in this way with $\Gamma = 0.5$, the model $\Omega = 1$ and $h = 0.5$ predicts a correlation function higher than that observed on scales of $\sim 10h^{-1}\text{Mpc}$ (Efstathiou et al. 1992). Therefore, Efstathiou et al. suggested replacing $\Gamma = 0.5$ with $\Gamma = 0.3$ in Eq. 5. We will call this *the CDM model* in this paper. Another possibility to get a lower Γ is to introduce a cosmological constant Λ so that $\Omega + \Omega_\Lambda = 1$. MCOR's simulation is based on such a model. We will use the same parameters and normalization as MCOR's, i.e. $\Omega = 0.4$, $\Omega_\Lambda = 0.6$, $h = 0.65$ and the present fluctuation variance 0.79 on the scale of $8h^{-1}\text{Mpc}$. We call this *the LCDM model*. We note that if the LCDM model is normalized by the COBE value, the fluctuation variance will be increased by approximately 30% and its fit to the observations will not be as good. All our simulations are performed equally for both the models.

The mean IGM temperature, which is $1 - 3 \times 10^4$ K between $z = 5$ and $z = 0$, can be calculated unambiguously when UV photo-ionization is the only heating source (Ostriker & Ikeuchi 1983). The thermal equation of state of the IGM is assumed to be polytropic, $T \propto n^{\gamma-1}$. In the linear evolution, one can prove that $\gamma = \frac{5}{3}$; in MCOR's simulation (their Fig. 7), we find this relation is best fit by $\gamma \simeq \frac{4}{3}$, which is also preferred in the calculation of Miralda-Escudé & Rees (1993). In addition, the lowest temperature in MCOR does not drop to zero, but is limited at the photo-ionization temperature $\sim 10^4$ K. We will use $\gamma = \frac{4}{3}$, the constant temperature $T_0 = 2 \times 10^4$ K at the mean density n_0 , and a minimum temperature 10^4 K to approximate the variation of T with n in the IGM. Our final results are very weakly dependent on the choice of γ or the minimum temperature. However, in the polytropic IGM, most mass resides in moderately high density regions where the temperature is considerably higher than T_0 . We should therefore use a density-averaged temperature T_m in the calculation of the Jeans length to account for this effect. Because $\delta_0(k) \propto T_m^{-1}$ at large k in Eq. 2, such a change is not trivial for the LCDM model, or at $z \leq 1$ in both models, when the clustering is strong. This introduces a factor of 2 (or even greater) difference between T_0 and T_m . For instance, if T_0 is used in the calculation of the Jeans length, the resultant σ of the IGM will be about 2.0 at $z = 3$ in the LCDM model; this is too large when compared to MCOR's value of 1.0.

Hydrogen atoms in the IGM are photo-ionized by the UV background radiation, which is assumed to be $J(\nu) = J_{21} \times 10^{-21} (\nu_0/\nu)^{1.5}$ ergs s^{-1} Hz^{-1} cm^{-2} sr^{-1} , where ν_0 is the frequency of the H I ionization threshold. The optical depth is proportional to the combination of J_{21} , Ω_b and h through $\frac{(\Omega_b h)^2}{h J_{21}}$; therefore, we fix Ω_b to the primordial density, $\Omega_b = 0.015h^{-2}$ (Walker et al. 1991), and let J_{21} be a free parameter.

The absorption optical depth at redshift z_0 is

$$\tau(z_0) = \int_{t_1}^{t_0} \sigma(\nu_\alpha \frac{1+z}{1+z_0}) n_{HI}(t) dt, \quad (6)$$

$$= \frac{cI_a}{H_0} \int_0^{y_1} dy \cdot n_{HI}(y) \cdot \frac{1}{\sqrt{\pi}(1+z)b} V(\alpha, \frac{z-z_0}{b(1+z_0)} + \frac{v(y)}{b}); \quad (7)$$

where σ is the absorption cross section at the Ly α transition, $y = xH_0/c$ is the normalized comoving coordinate, $I_a = 4.45 \times 10^{-18} \text{ cm}^2$, V is the standard Voigt function, $b = \sqrt{2kT/mc^2}$ and $v(y)$ is the peculiar velocity measured in units of c . There are two major effects of the velocity: 1) shifting lines to slightly different position and 2) altering line profiles by bulk motions through velocity gradients. The first effect is not important if we are not interested in clustering properties of lines. The second effect can make lines narrower, since in comoving space mass is falling toward the center of the cloud. Only clouds with $N_{HI} \leq 10^{11} \text{ cm}^{-2}$ are expanding in comoving space (see §3.3) and consequently have broader line profiles, but these lines are not observable. In the present paper, we will use the linear estimate for the peculiar velocity. The success of the Zel'dovich approximation indicates that the velocity can be described by linear theory in the early non-linear stages. (Note the velocity is the first derivative of the potential and the density is the second derivative).

2.2. Simulation method

Here is the summary of the simulation procedure. We first simulate $\delta_0(k)$ and $v(k)$ in a line of sight at discrete $k_i, i = 1, 2, \dots, N$ in the Fourier space. They are two correlated Gaussian random fields and can be written as linear combinations of two independent Gaussian fields $w(k)$ and $u(k)$ of power spectra $P_w(k)$ and $P_u(k)$, respectively (see Bi 1993 and Bi, Ge & Fang 1995) :

$$\delta_0(k, z) = D(z)(u(k) + w(k)), \quad (8)$$

$$v(k, z) = F(z) \frac{H_0}{c} i k \alpha(k) w(k), \quad (9)$$

where $D(z)$ and $F(z)$ are the linear growth factors for δ_0 and v at redshift z (Peebles 1993).

Functions α , P_w and P_u are :

$$\alpha(k) = \frac{\int_k^\infty P_{IGM}(q) q^{-3} dq}{\int_k^\infty P_{IGM}(q) q^{-1} dq}, \quad (10)$$

$$P_w(k) = \alpha^{-1} \int_k^\infty P_{IGM}(q) 2\pi q^{-1} dq, \quad (11)$$

$$P_u(k) = \int_k^\infty P_{IGM}(q) 2\pi q dq - P_w(k), \quad (12)$$

with $P_{IGM}(k) = P(k)/(1 + x_b^2 k^2)^2$ being the present 3-D power spectrum of the IGM. The corresponding distributions in the real line-of-sight space can be obtained by using a Fast Fourier Transform. Typically, $N = 2^{14} = 16384$ and the length of the simulation is $\Delta z = 0.2$ in redshift, corresponding to the grid size $4.5 h^{-1}\text{kpc}$ and the simulation box size $75 h^{-1}\text{Mpc}$ in comoving space at $z = 3$ in the $\Omega = 1$ model. The grid is fine enough to reveal detailed structures in clouds. The box length is long enough to incorporate most fluctuation powers. Greater N (e.g. 2^{16}) has

also been tested with no difference found. The neutral hydrogen density n_{HI} and the Ly α optical depth are calculated directly at each grid point according to our assumption of photo-ionization equilibrium and Eq. 6. Specifically, the neutral fraction is

$$f(T, J_{21}, n_e) = \frac{\alpha(T)}{\alpha(T) + \Gamma(T) + G_1 J_{21}/n_e}, \quad (13)$$

where $G_1 = 2.83 \times 10^{-12}$ for a UV spectrum with power-law index -1.5, $\alpha(T)$ is the recombination rate, $\Gamma(T)$ the collisional ionization rate, and n_e the number density of electrons (e.g. Black 1981). The detailed UV spectrum of Haardt & Madau (1995) predicts $G_1 = 3.2 \times 10^{-12}$, almost the same as the pure power law.

We create a reference density field by filtering $n_{HI}(y)$ with a Gaussian function with dispersion b_m , with b_m in the range 0 to $(2kT_m/m_p)^{\frac{1}{2}}$. Then we define each region between two successive minima in the reference field as an *absorber* or *cloud*, and each maximum between the minima as the central position of the absorber. The reference field is used only for the purpose of defining a *boundary*. It is not used even for defining the physical size of a cloud. Statistical properties of clouds that will be defined in Section 3.2 are always calculated directly from the original n_{HI} . With $b_m = 0$ (“no smooth”), the reference field is identical to n_{HI} and we will select every feature in n_{HI} as a separate cloud. With $b_m = (2kT_m/m_p)^{\frac{1}{2}}$ (“maximal smooth”), density features on scales much smaller than the thermal broadening are erased and the clouds identified match best to real Voigt lines in QSO spectra. The reason for smoothing the reference field is twofold. First, we should not include any sparse enhancement over the local background density profile of an absorber as a new absorber. And second, any fine structures that have been smoothed out by b_m may be unobservable because of thermal broadening, so we should let the term “cloud”, which usually implies “one line” in the spectrum, refer to just “one region” in space. We find that b_m with “maximal smooth” can be applied to moderately resolved QSO spectra, while b_m with “no smooth” may be applied to very highly resolved spectra like Keck observations.

The optical depth is calculated directly from n_{HI} and has nothing to do with this selection procedure for identifying clouds.

3. Properties of the IGM and Ly α Clouds

3.1. Global evolution of mass and volume filling factors

The LN field describes a density evolution in which mass moves slowly to high-density regions while more and more volume is left with low densities. Denote $\rho = n/n_0$ and σ^2 the variance of the linear density; the fraction of volume $V(> \rho)$ occupied by densities above a given ρ and the associated mass fraction $M(> \rho)$ are, respectively,

$$V(> \rho) = \int_{\rho}^{\infty} p(\rho) d\rho = \frac{1}{2} \operatorname{erfc} \left(\frac{\sigma}{2\sqrt{2}} + \frac{\ln(\rho)}{\sqrt{2}\sigma} \right); \quad (14)$$

$$M(>\rho) = \int_{\rho}^{\infty} \rho p(\rho) d\rho = \frac{1}{2} \operatorname{erfc}(-\frac{\sigma}{2\sqrt{2}} + \frac{\ln(\rho)}{\sqrt{2}\sigma}); \quad (15)$$

where $p(\rho)$ is the one-point distribution function of ρ , and the variance of ρ is $\exp(\sigma^2) - 1$. We have plotted these functions at selected redshifts from $z = 40$ to $z = 0$ in Fig. 1 for the CDM model. Fig. 2 shows the evolution of the volume $V(\rho < 1)$ (solid line) occupied by densities less than the mean and their associated mass fraction $M(\rho < 1) = 1 - V(\rho < 1)$ (dashed line), and the volume $V(\rho < 0.5)$ and the associated mass $M(\rho < 0.5)$.

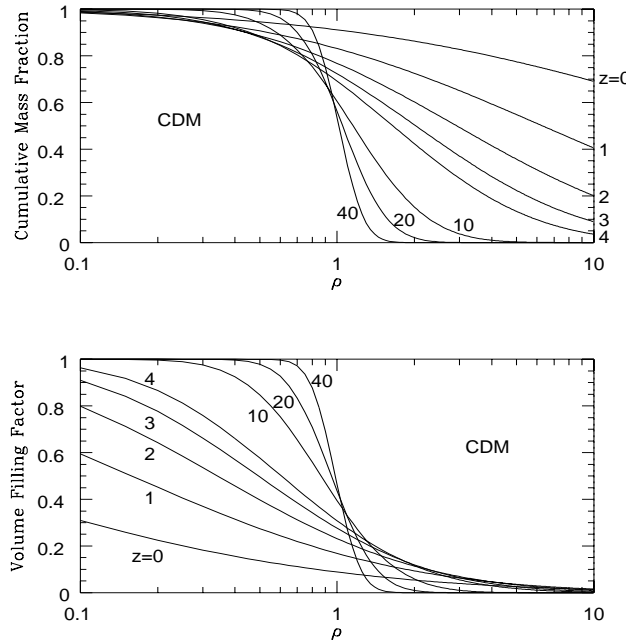


Fig. 1.— Cumulative mass fractions and volume filling factors from mass densities in the IGM above a given density threshold $\rho \equiv \frac{n}{n_0}$ at redshifts $z = 40, z = 20, \dots$, to $z = 0$ in the CDM model. These curves are derived from our hypothesis that the probability distribution function of the intergalactic gas density is given by the lognormal distribution.

The different curves in Fig. 1 are determined uniquely by the standard deviation σ , which is plotted in Fig. 3. The solid line in the figure is for the CDM model and the dashed line for the LCDM model. Some specific values for the CDM model are $\sigma = 0.87$ at $z = 5$, 1.00 at $z = 4$, 1.18 at $z = 3$, 1.47 at $z = 2$ and 1.90 at $z = 1$. For comparison, $\sigma = 1.0$ at $z = 3$ in MCOR. Using numerical simulations in a cold dark matter model with the power spectrum 1.4 times smaller than ours, Carlberg & Couchman (1989) obtained $\sigma = 0.744, 0.953, 1.39$ and 1.44 at $z = 4.63, 2.80, 1.36$ and 0.81 for the linear IGM (see Table 2 of Miralda-Escudé & Ostriker 1990). These values are consistent with our calculations.

At $z = 3$, the IGM in our model is just a median fluctuated field in which both overdensities

and underdensities have considerable filling factors and are significant in appearance. Yet there is still enough contrast to cause line-like absorption. In the very early universe ($z > 10$), half of the volume is occupied by gas whose density is below the mean, with about half of the total mass contained. As the fluctuations increase, mass moves into overdensities above the mean. Fig. 1 shows that at redshift 4, only 30% of the mass is in the underdense regions, but this mass occupies 70% of the volume. At redshift 1, this becomes $\sim 20\%$ of the mass in $\sim 80\%$ of the volume.

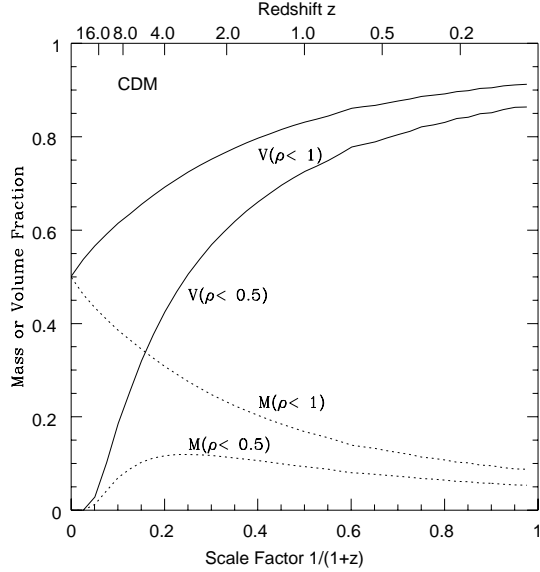


Fig. 2.— The solid curves show the evolution of volume filling factor vs. the scale factor $a = (1 + z)^{-1}$ in the CDM model for gas at densities $\rho \leq 0.5$ or $\rho \leq 1.0$. The dotted curves show the mass fractions at these densities.

As we will see in §3.2, a typical Ly α cloud at $z = 3$ with $N_{HI} = 10^{13.5} \text{ cm}^{-2}$ will have a density approximately equal to the mean, $\rho = 1$, and an $N_{HI} = 10^{12.0} \text{ cm}^{-2}$ absorber has $\rho = 0.2$; therefore the clouds between $10^{12.0}$ and $10^{13.5} \text{ cm}^{-2}$ are *underdense*!

We have made similar plots to those in Fig. 1 for the LCDM model, but the difference is almost invisible because the variance is so similar in the two models, as shown in Fig. 3. For example, $\sigma = 1.25$ at $z = 3$, compared to 1.18 in the CDM model. Therefore, we have not repeated the figures again. In fact, we find most of the statistical quantities are identical in both the models, so they will be illustrated for the CDM model only. In this paper, if it is not stated explicitly, the LCDM model may always be assumed to have essentially the same plots as the CDM model.

3.2. Photo-ionization of the IGM

At temperatures of $10^3 - 10^5 \text{ K}$, the only significant ionization process in the IGM is photo-ionization. The relation between the neutral fraction and the density is shown for the CDM

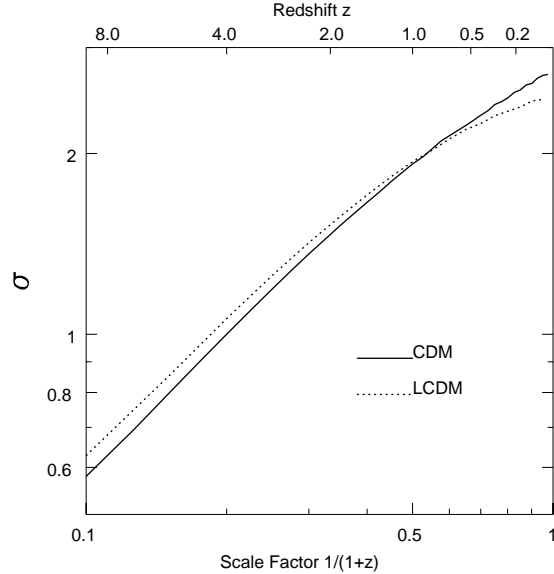


Fig. 3.— The growth of fluctuations in the IGM vs. the scale factor. The variance of the linear fluctuation is σ^2 , while the variance of the density distribution of the LN model is $\exp(\sigma^2) - 1$. The evolution of σ is shown as a solid curve for the CDM model, and a dotted curve for the LCDM model.

model in Fig. 4a at redshift $z = 2$ (solid line), 3 (dotted line) and 4 (dashed line) using $J_{21} = 0.18$ with $\Omega_b = 0.015h^{-2}$, or $J_{21} = 0.50$ with $\Omega_b = 0.025h^{-2}$. (The LCDM model gives the same results with the same J_{21} .)

Let's define a few physical parameters of neutral hydrogen absorbers.

The column density N_{HI} of an absorber is obtained by summing neutral densities in each pixel from the first minimum to the next minimum in the reference field. The column density of *total* hydrogen can be calculated in the same way. The ratio between the neutral and total column densities defines the neutral fraction of the cloud.

The mean density of a cloud is the density-weighted density in each pixel : $\langle \rho \rangle = \frac{\sum n_i^2}{n_0 \sum n_i}$. Because in photoionization equilibrium the neutral density is proportional to the square of the total density, this mean density can be calculated in another way, namely the density deduced from the neutral fraction in Fig. 4a. Note that both the column density and the mean mass density are defined independently of any detailed structure of the cloud, and also independent of the starting and ending points of the region outlined by the reference field; this is because most of the mass is contained sharply around the center of the density fluctuation.

The size D of a cloud is defined to be the total column density divided by the mean density. This is just a convenient representation of the scale over which the absorber's 3-D density is typically measured. It may or may not be equal to the real diameter of the cloud even if it happens

to be a sphere, but they should be close to each other.

The physical “radius”, which is taken to be half of the cloud size, is plotted in Fig. 4b with light curves for the CDM model and heavy curves for the LCDM models after averaging over 1000 random realizations. As a comparison, the physical Jeans radius, i.e. half of the Jeans length λ_b , is 0.13, 0.075, and 0.051 $h^{-1}\text{Mpc}$ at $z = 2, 3$ and 4 in the CDM model, and 0.21, 0.13, and 0.082 $h^{-1}\text{Mpc}$ in the LCDM model. We note that the radius increases slowly with increasing column density. This is expected when clouds have no boundaries. The radius for $N_{HI} = 10^{14} \text{ cm}^{-2}$ at $z = 2$, which is 110 $h^{-1}\text{kpc}$ in the CDM model, is consistent with that measured for the paired Q1343+266 A, B where the best fit value is around 90 $h^{-1}\text{kpc}$ (Bechtold et al. 1994; and Dinshaw et al. 1994). The radius in the LCDM model is always larger than that in the CDM model because of the different cosmological geometry. If the universe is the flat LCDM model, the detected radius of clouds will be larger than for the $\Omega = 1$ CDM model. Simulations of such paired spectra can be found in Bi (1993) and Charlton et al. (1996).

The mean density of clouds is plotted vs. their neutral column densities in Fig. 4c. As expected for photo-ionization, the density is proportional to the square root of the column density. The column densities that correspond to the mean density are $10^{12.9} \text{ cm}^{-2}$ at $z = 2$, $10^{13.4} \text{ cm}^{-2}$ at $z = 3$ and $10^{13.9} \text{ cm}^{-2}$ at $z = 4$. It is perhaps surprising to see that these clouds are those that appear most commonly in the Ly α forest, yet they have just the mean density of the universe. Fig. 4d plots the neutral fraction at various column densities. One can see that high density clouds have a higher neutral fraction. These curves can be compared with Fig. 9b of MCOR. The agreement is good in general.

We have tabulated the total baryonic mass $\rho n_0 m_p D^3$, and the Jeans mass $n_0 m_p \lambda_b^3$ in Table 1 in units of $\log_{10}(M/M_\odot)$. Fig. 5 shows the mass vs. column density at $z = 2, 3$ and 4. Mass clumps of the constant fluctuations $\rho = 10, 1$, and 0.2 have been traced by the dashed arrows. The Jeans mass is marked as M_J in the figure. The marked mass, M_3 , is an example of a specific cloud found in our simulation, which we will discuss in detail in §5.2.

The meaning of the mass for low column density clouds should be interpreted with caution. They most likely originate from different impact parameters, and so represent only small parts of larger absorbers.

3.3. Structures within clouds

The line-of-sight distributions of peculiar velocity and neutral density *within* clouds have been plotted (as the solid curves) vs. the comoving separation from the center of cloud in the CDM and LCDM models in Fig. 6 at $z = 3.0$. The successive curves with increasing peak values are mean profiles of all clouds between $10^{11} \rightarrow 10^{12} \text{ cm}^{-2}$, $10^{12} \rightarrow 10^{13} \text{ cm}^{-2}$, ..., $10^{15} \rightarrow 10^{16} \text{ cm}^{-2}$ correspondingly. The dashed curves show the same plots if we do not use the smoothed reference field to select clouds, but count *any* maximum in the density distribution as one cloud.

The peculiar velocity shows that mass is falling toward the cloud centers in comoving space except for $N_{HI} < 10^{12} \text{ cm}^{-2}$. For clouds with $N_{HI} = 10^{13} - 10^{15} \text{ cm}^{-2}$, the bulk velocities are just comparable to the thermal broadening; for clouds with $N_{HI} = 10^{11} - 10^{13} \text{ cm}^{-2}$, they are negligible. Hence, most strong lines will have sharpened profiles due to the infall velocity. The maximal effect occurs at a separation of about 0.2 to 0.4 $h^{-1}\text{Mpc}$, depending on the column density. The velocity is also larger in the LCDM model than in the CDM model at the same column density.

Below $10^{15.5} \text{ cm}^{-2}$, the peculiar velocities are smaller than the Hubble velocity at all distances; therefore, at $z = 3$ the clouds are still expanding in proper coordinates, although in comoving space, they are condensing. The neutral column density, which is proportional to the square of the proper density of total mass, decreases with cosmic time. Thus the same cloud will have a higher column density at $z = 4$ than at $z = 2$. This will also be shown with examples in §5.1. In this sense, none of the forest clouds is confined in proper space. Only for $N_{HI} \geq 10^{15.5} \text{ cm}^{-2}$, have we found stable or even collapsed clouds in proper space on the scale of $\sim 0.1h^{-1}\text{Mpc}$. However, these clouds are very rare in the present simulation.

We find that the neutral hydrogen density profile of a cloud as illustrated in Fig. 6 is well described as

$$n_{HI}(x) = \frac{N_{HI}}{x_0} \exp\left(-\frac{x}{x_0}\right), \quad (16)$$

where $x_0 = 0.14h^{-1}\text{Mpc}$ for the CDM model, or $0.20 h^{-1}\text{Mpc}$ for the LCDM model. We note this x_0 is close to x_b in Eq. 2; therefore, the density declines exponentially outside the Jeans radius. If we take all maxima in the density distribution as separate clouds, the cloud sizes and peculiar velocities become about half as large, but their spatial structures (i.e. the dashed curves) are similar.

An important point is that not only the velocity but also the exponential density profile, which extends far away from the center of a cloud without a cut-off, will affect absorption line profiles. We call this *the absorption from density wings*. For instance, in the CDM model, a cloud with $N_{HI} = 10^{14.5} \text{ cm}^{-2}$ will have $n_{HI} = 6 \times 10^{-12} \text{ cm}^{-3}$ at $0.8 h^{-1}\text{Mpc}$, which is comparable to the peak density of a typical $N_{HI} = 10^{12.5} \text{ cm}^{-2}$ cloud. Therefore, the wing density at $0.8 h^{-1}\text{Mpc}$, or 137 km s^{-1} in velocity at $z = 3$, is still contributing a noticeable absorption depth, since the $10^{12.5} \text{ cm}^{-2}$ column density is just detectable in observations. The resulting Ly α profile is thus much *broader* than the pure Voigt profile of the cloud at the same column density but with all mass at its center. This effect exists in all clouds. As a short summary, the velocity sharpens lines at column density above $10^{13.5} \text{ cm}^{-2}$, but the wing absorption broadens lines in the same way for all absorbers. Hence, we have three kinds of departures from the Voigt profile : the density wing, the peculiar velocity and the line-blending effect.

In real observations, the column density and velocity fitted by multiple Voigt profiles will be significantly different from the intrinsic column density because of line-blending and fluctuations. For an arbitrary absorber, it is almost impossible to say which effect – the internal temperature,

the peculiar velocity, or the density wing – plays the most important role. An exception is for *isolated* clouds with $N_{HI} \leq 10^{13} \text{ cm}^{-2}$: they are on the linear part of the curve-of-growth and thus have unchanged N_{HI} ; but their b parameters will be significantly boosted by the wing absorption.

How the fitted parameters differ from actual parameters will deserve a careful statistical study. Unfortunately, available Voigt fitting software is very slow; we have not made extensive calculations for the present paper. A real Voigt fitting of a particular simulation sample will be illustrated in §5, however.

4. Global evolutions of HI Opacity and dN/dz

We discuss the redshift evolution of the hydrogen Ly α opacity τ_{HI} and the number density of clouds dN/dz in this section. The optical depth is proportional to the factor $\mu = \frac{(\Omega_b h^2)^2}{h J_{21}}$. When Ω_b is fixed to the nominal primordial value, all uncertainties of the factor can be attributed to J_{21} . There is a number of τ_{HI} observations at $z \geq 1$ from which we need one at a particular redshift to normalize J_{21} . The evolution of the opacity at other redshifts should then be automatically generated by the IGM model. We choose $z = 2.4$ because this is the mean redshift where the Hopkins Ultraviolet Telescope has measured the helium opacity toward HS1700+64 (DKZ) and for which there is also a good hydrogen Ly α spectrum observed by Keck (Tytler 1995; Zheng et al. 1996).

The average Ly α opacity at $z = 2.4$ is 0.153 according to the recent measurement of Dobrzański & Bechtold (1996). The opacity for HS1700+64 is 0.22 ± 0.01 (Davidsen et al. 1996). The difference presumably comes from random statistics, i.e. fluctuations in the number of intercepted clouds due either to variation in the density or the UV background, or both. The global value $\tau_{HI} = 0.153$ will be adopted in the following discussion. When comparing synthetic samples directly to the Keck spectrum of HS1700+64 in §5, we will use 0.22. Fig. 7 plots τ_{eff} versus J_{21} at $z = 2.4$, where

$$\tau_{eff} = -\ln \left\langle \frac{I_{obs}}{I_0} \right\rangle \quad (17)$$

is the effective opacity measured over a sufficiently large spectral range (243Å in our simulation). Two values of Ω_b , $0.025h^{-2}$ and $0.015h^{-2}$, are illustrated. The UV flux, $J_{21} = 0.50$ or 0.18 that we have adopted in the last section has been selected for $\Omega_b = 0.025h^{-2}$ or $0.015h^{-2}$, respectively, because the resulting HI opacity is 0.155 in both the models.

The UV flux $J_{21} = 0.18$ is lower than what is typically inferred from the QSO proximity effect, $J_{21} = 10^{\pm 0.5}$ (Bajtlik, Duncan & Ostriker 1988; Lu, Wolfe & Turnshek 1991; Bechtold 1994). However, it is consistent with the results of hydrodynamical simulations (e.g. Cen et al 1994; MCOR; Zhang et al. 1995; Hernquist et al. 1996). The flux $J_{21} = 0.5$ is the value obtained for the observed quasars at $z = 2 - 3$ (Haardt & Madau 1996). A recent study of the proximity effect suggests $J_{21} = 1.0_{-0.3}^{+0.5}$ (Cooke, Espey & Carswell 1996).

If the IGM is uniform and J_{21} is constant with z , the opacity will be proportional to $(1+z)^{4.5}$ (Jenkins & Ostriker 1991). In a clumpy IGM, there are two opposing effects due to clumping. First, the neutral density, which is proportional to the square of the total density (in the isothermal case), is increased by the clumping factor, and so is the opacity. Second, clouds of $N_{HI} \geq 10^{14} \text{ cm}^{-2}$ will be saturated in the curve-of-growth, so mass clustered into those clouds contributes much less to the absorption. The results of our calculation are plotted in Fig. 8, where the observations of Dobrzycki & Bechtold (1996),

$$\tau_{HI}(z) = 0.153 \times \left(\frac{1+z}{3.4}\right)^{3.33}, \quad (18)$$

are illustrated (with $\sim 30\%$ variations) as the shaded region. The two heavy curves are for the CDM (solid) and LCDM (dotted) models, respectively, which are best fitted by $\tau = 0.26[(1+z)/4]^{1+\gamma}$ with index $\gamma = 2.1$. The corresponding light curves are for the case of a uniform IGM with the same mean density. The three solid points are the simulation results of MCOR. The two effects of clustering compensate with each other at redshift 2.0, giving an effective opacity which is the same for the clumpy IGM as it would be for a uniform IGM of the same mean density. At lower redshift, the first effect dominates but at higher redshift, the second effect dominates. Consequently we obtain more opacity at low redshift and less opacity at high redshift than what is expected for a uniform IGM. The power law of the evolution is thus changed from index 3.5 to 2.1 in our simulation. The agreement between the observations and the model is acceptable with a constant UV flux for $z = 2 - 4$; evolution of J_{21} over this range of redshifts is therefore not required.

Most of the hydrogen opacity originates from clouds of column density greater than 10^{13} cm^{-2} , with total mass density close to or above the universal mean density. Hence they contain most of the mass too. To show this fact more clearly, we have plotted the cumulative mass fraction for clouds *above* a given column density in Fig. 9a for $z = 2, 3$ and 4 in the CDM model. The cumulative HI opacities are plotted in Fig. 9b, and the cumulative number of clouds per unit redshift are shown in Fig. 9c. There is very little contribution to the HI opacity from clouds below 10^{13} cm^{-2} because of their negligible total mass, which is quite consistent with the studies where absorbers are treated as discrete clouds. The mass and the HI opacity are proportional to each other in the model. However, there is not a one-to-one correlation between the total number of clouds and the opacity. While only a few clouds are found below 10^{13} cm^{-2} at $z = 4$, there exists a large number of low column density clouds at $z = 2, 3$ in Fig. 9c. Fig. 9d is a plot of the differential column density distribution. MCOR made the same plot as their Fig. 15b. The straight line is a power law of index -0.5 that corresponds to $\beta = -1.5$ in the traditional $d^2N/dzdN_{HI} \propto N_{HI}^{-\beta}$ function.

The evolution of the column density distribution versus redshift is apparent; the difference cannot be explained simply by a factor in the amplitude. The three curves at $z = 2, 3$ and 4 can be shifted to overlap each other in the x-axis. This shows an important fact : that the evolution of the Ly α forest is not due to creating or destroying of new clouds, but due to a *change of column density in the same clouds*. Because of the expansion of the universe, clouds have smaller mass

density (and neutral density) at low redshifts than at high redshifts. An interesting conclusion is that there are more 10^{12-13} cm $^{-2}$ absorbers at $z = 2$ than at $z = 4$. This may be tested by future Keck observations. See Fig. 15b of MCOR for a similar conclusion.

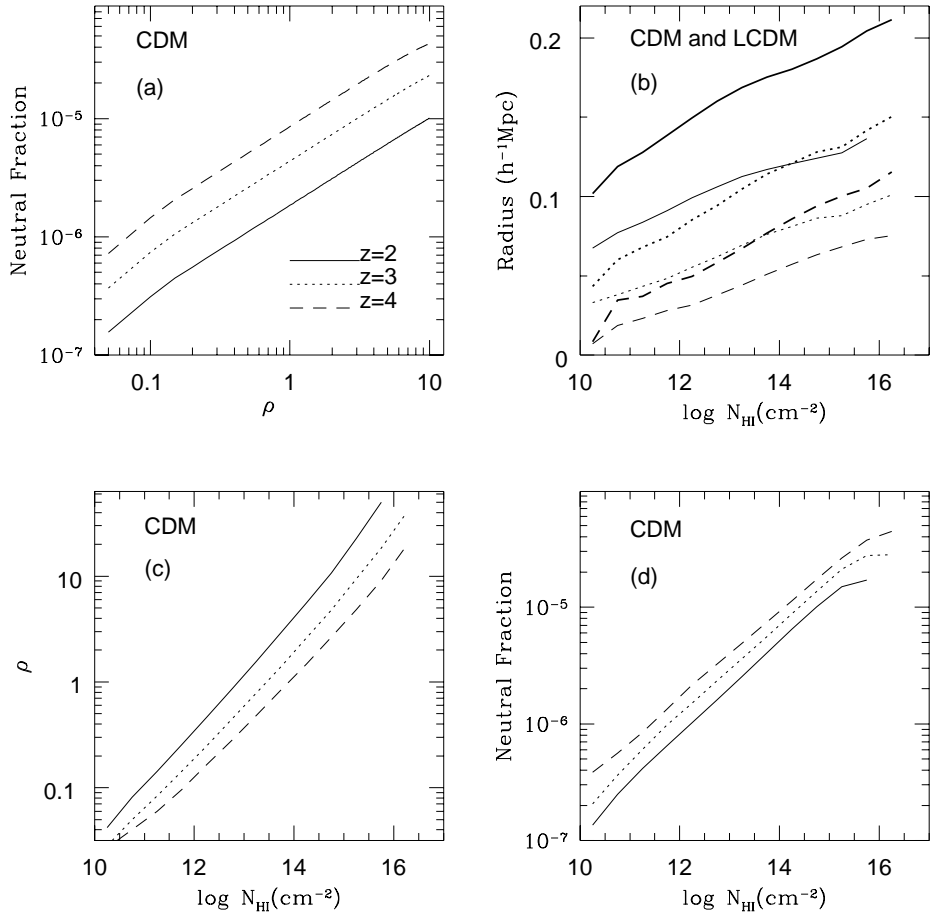


Fig. 4.— **(a)** the neutral fraction vs. the density ρ in the IGM at three different redshifts : $z = 2$ (solid), $z = 3$ (dotted) and $z = 4$ (dashed) in the CDM model. **(b)** the physical “radius” (see text) of Ly α absorbers at different column density. The light and heavy curves are for the CDM and LCDM models, respectively. Figs. 4c and 4d show the mean density and neutral fraction vs. the column density.

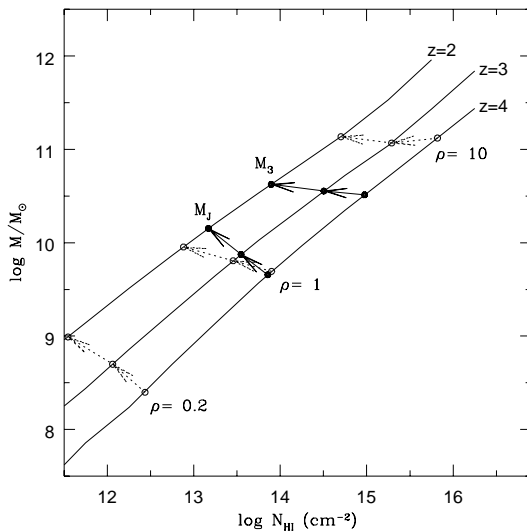


Fig. 5.— Average baryonic mass of Ly α absorber vs. column density at $z = 2, 3$ and 4 in the CDM model. The absorbers at the constant density $\rho = 0.2, 1.0$ and 10 are traced as dashed arrows and open circles. The Jeans mass M_J is marked with solid points. The solid points for M_3 trace the specific cloud No. 3 discussed in §5.3.

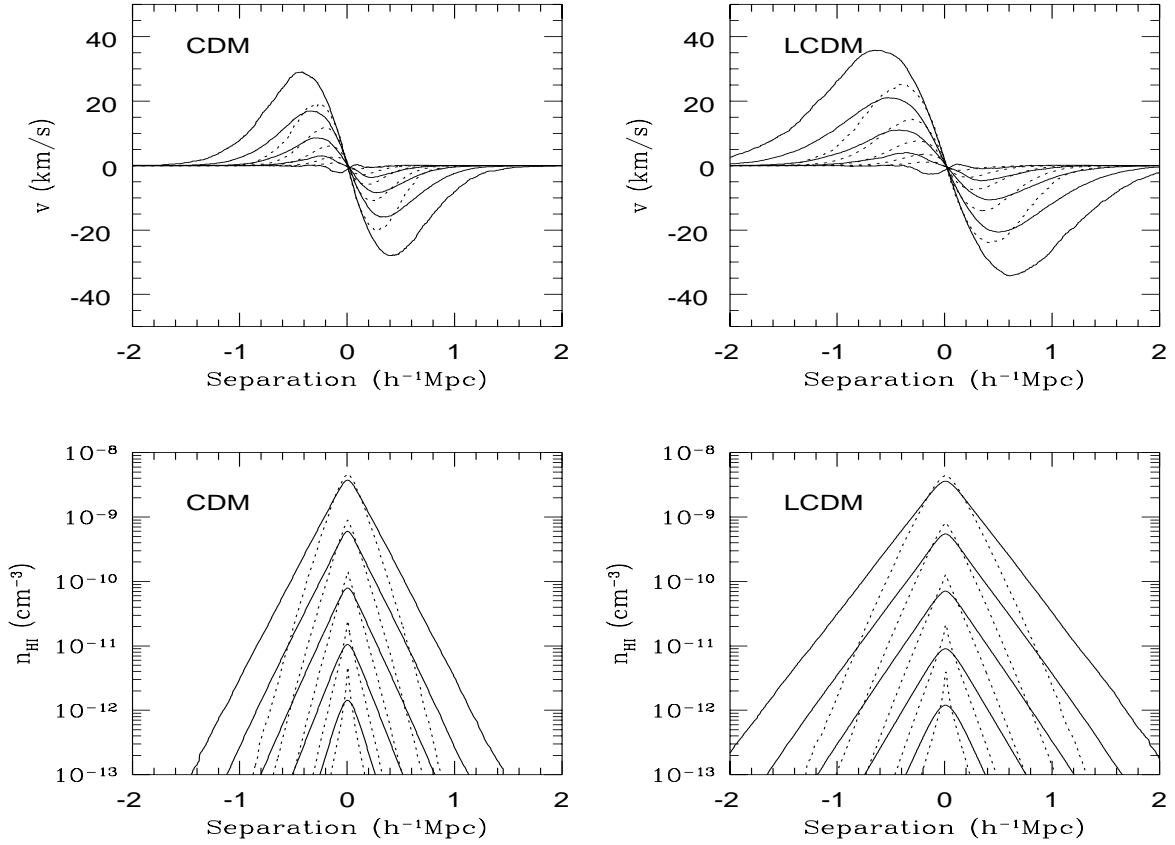


Fig. 6.— Averaged density and peculiar velocity profiles vs. comoving radius from the center of a cloud are plotted as solid curves in both the CDM and LCDM models, using the selection procedure in §3.1. The curve with the highest amplitude corresponds to the cloud at $N_{HI} = 10^{15.5} \text{ cm}^{-2}$ and the successive curves with lower amplitudes are at $N_{HI} = 10^{14.5}, 10^{13.5}, 10^{12.5}$ and $10^{11.5} \text{ cm}^{-2}$, respectively. Absorbers are selected according to the “maximal smooth” procedure. If we select *any* individual maxima in the line-of-sight density distribution in the IGM as separate clouds, i.e. with the “no smooth” procedure, the cloud dimensions and the peculiar velocity become smaller, which are plotted as the dotted curves.

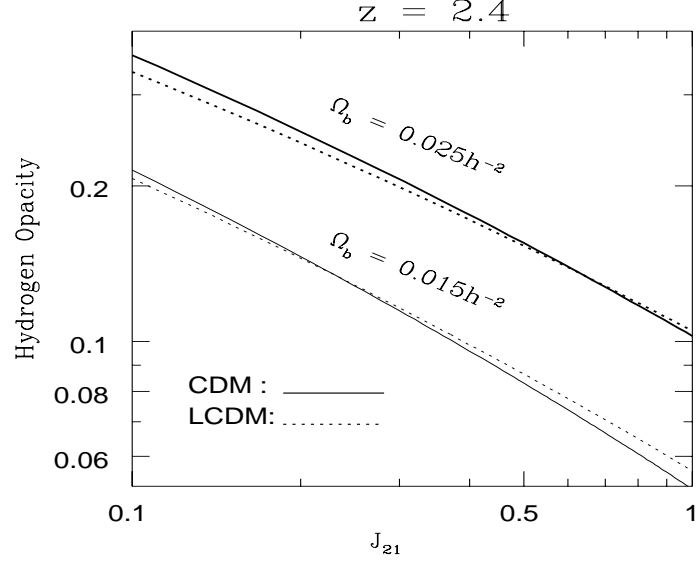


Fig. 7.— The effective HI opacity at $z = 2.4$ vs. the UV background flux J_{21} for two different cosmological baryon densities : $\Omega_b = 0.025h^{-2}$ and $\Omega_b = 0.015h^{-2}$. The solid and dashed curves are for the CDM and LCDM models, respectively.

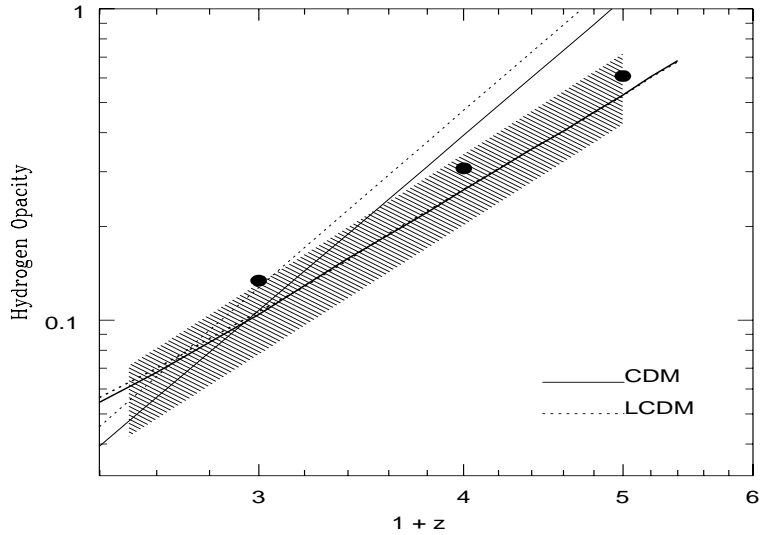


Fig. 8.— Evolution of the effective hydrogen opacity from redshift 4 to redshift 1.6 in the CDM (heavy solid line) and LCDM (heavy dotted line) models, both of which can be fitted by the power law $\tau \propto (1+z)^{3.1}$. The ionizing background intensity is assumed to be constant. The corresponding light-weight curves, $\tau \propto (1+z)^{4.5}$, are what is expected for a uniform IGM with the same mean density. The shaded region is the observational curve $\tau_{eff} = 0.153(\frac{1+z}{3.4})^{3.33}$ with 30% variations from Dobrzycki & Bechtold (1996). The three solid points are from MCOR's simulation.

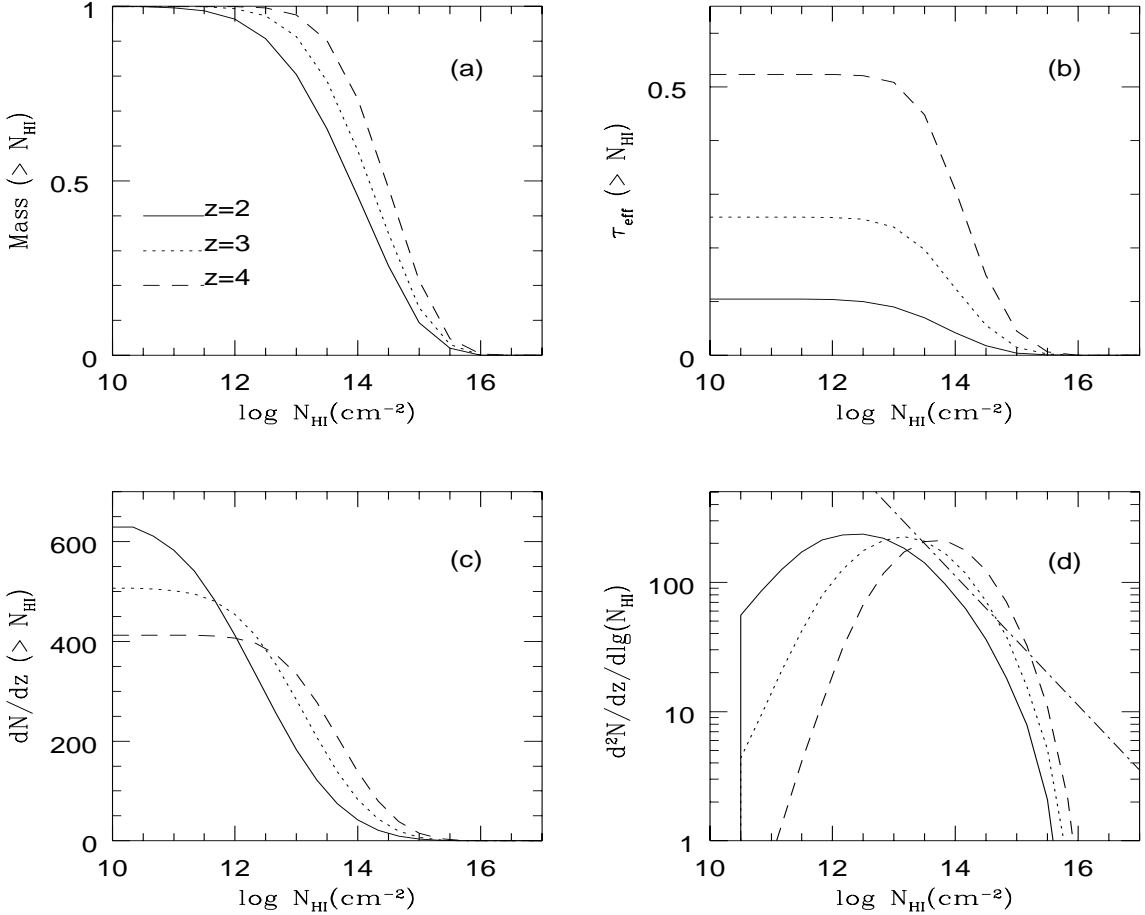


Fig. 9.— The cumulative mass fraction, HI opacity, and number of clouds per redshift above a given column density are illustrated in Figs. 9a, 9b and 9c, respectively, for three redshifts $z = 2$ (solid), $z = 3$ (dotted) and $z = 4$ (dashed) in the CDM model. Fig. 9d is the number of clouds per redshift per $\log N_{HI}$. The dot-dashed curve is a power law of index -0.5.

The column densities here are intrinsic values, i.e., calculated directly from the neutral hydrogen distribution. In real observations, Ly α lines are blended so that both the number of lines and the column densities in a blended absorption spectrum depend on the resolution and signal-to-noise ratio of the observation. This “blending effect” will introduce a correction factor between the number of intrinsic clouds and the number of observational lines fitted according to various Voigt profiles. The best way to solve this difficulty is to fit simulated spectra in the same way as observations. However, the well-known Voigt fitting software, VPFIT, is too slow to be useful because the simulation data set is huge. In section §5.1, we have run VPFIT to one of the simulation samples at $z = 2.4$ and have found that the number of intrinsic clouds is about 1.70 times larger than the number of lines found in the simulated spectrum and fitted by Voigt profiles in $12.5 \leq \log N_{HI} \leq 15.0$. Fig. 10 shows the column density distribution $f(N)$ in units of counts per column density per X , where $X = 0.5(1+z)^2 - 1$. The relation between $f(N)$ and $\frac{d^2N}{dzdN}$,

the counts per column density per redshift, is $f(N) = \frac{d^2N}{dzdN}/(1+z)$. The solid data points are from the raw data of 4 Keck spectra (Hu et al. 1995), and the error bars are from the earlier statistical results (Petitjean et al. 1993). Two power laws are plotted. The dot-dashed straight line is the power law of index -1.46 and the short dashed line of index -1.80, which fit to the observational data below 10^{14} cm^{-2} and above 10^{14} cm^{-2} respectively. The light solid curve is from the CDM model using “maximal smooth” (the reference field is smoothed on the scale of the thermal dispersion), and the heavy long-dashed curve using “no smooth” (every feature in the neutral hydrogen distribution is regarded as a separate cloud). The corresponding curves in the LCDM model are almost the same. The factor 1.70 mentioned above has been applied to correct the number of clouds in the simulation to the number of lines expected.

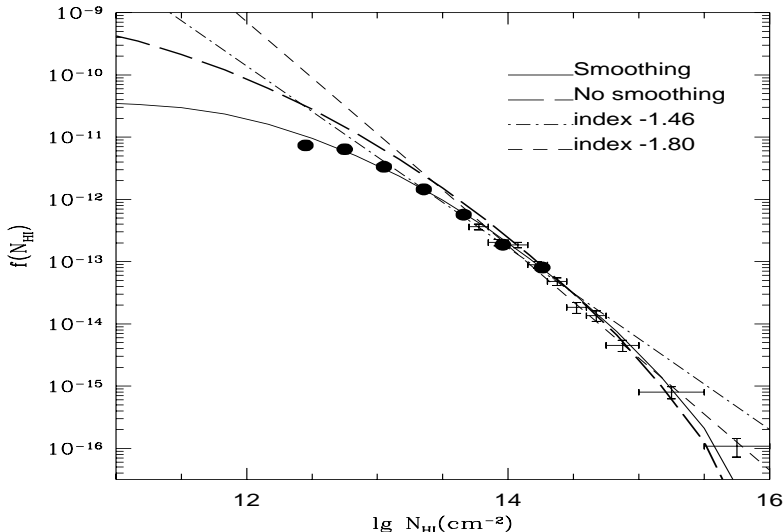


Fig. 10.— Probability distribution of column density defined as counts per column density per X with $X = 0.5(1+z)^2 - 1$. The original observations are plotted as dot points from Hu et al. (1995) and error bars from Petitjean et al. (1993). The dot-dashed and short dashed straight lines are power laws of index -1.46 or -1.80, respectively. The light solid curve is from the CDM model using the “maximal smooth” procedure in §3.1. The heavy long dashed curve is without smoothing (the “no smooth” procedure). The factor of 1.70 has been taken into account relating the number of intrinsic clouds and the number of clouds derived in the Voigt fit to the simulated spectra (see §5.1).

The CDM model matches the Keck result quite well in the range $13.0 \leq \log N_{HI} \leq 14.0$. Below $10^{13.0}$, some Ly α lines would be missed even in the Keck data. Our smoothing procedure in the cloud selection has underestimated the counts too, apparently because such small features are easier to be erased. The distribution $f(N)$ from clouds without smoothing can fit the “original” counts of clouds at $\log N_{HI} \leq 13.0$, which is suggested to fit the power law with $\beta = -1.46$ in the figure (Hu et al. 1995). At somewhat higher column densities the distribution steepens,

giving $\beta = -1.80$ over the range $14.0 \leq \log N_{HI} \leq 15.5$, and matching the results of Petitjean et al. (1993). At $\log N_{HI} \geq 16.0$, we find almost no clouds in the simulation, indicating that these absorption systems have other physical origins than do the ordinary Ly α forest clouds. We associate these Lyman limit systems and the even higher column density damped Ly α systems with collapsed objects, such as galactic disks. These much rarer high column density systems are clearly highly non-linear and would not be expected to be produced in our calculation.

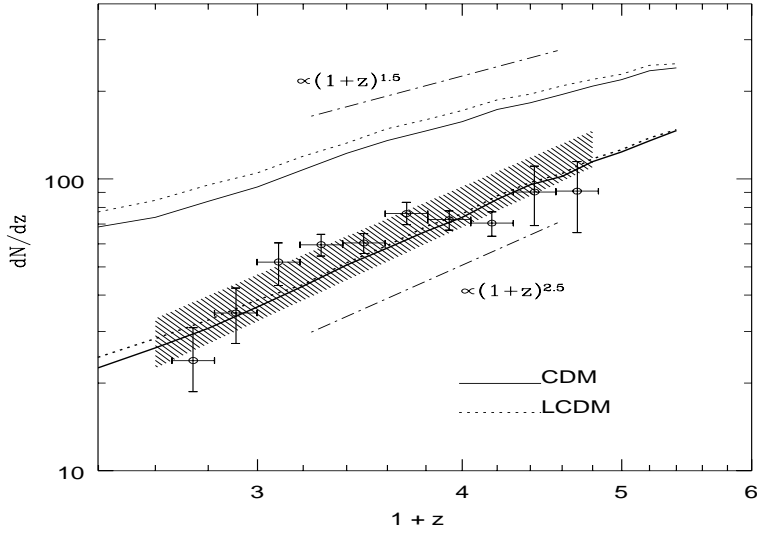


Fig. 11.— dN/dz for $W_0 \geq 0.32\text{\AA}$. The data points are from Bechtold (1994) and the shaded region is the fit formula with 30% variations from Lu, Wolfe & Turnshek (1991). The heavy solid and dotted curves are for the CDM and LCDM models, respectively, both of which are best fitted by a power law $\propto (1+z)^{2.5}$. The light curves are dN/dz for Ly α lines selected with their minimum transmitted fluxes below 0.5, which are best fitted by $\propto (1+z)^{1.5}$.

For each simulated spectrum, lines are selected from two successive maxima and their equivalent widths are calculated directly. The resulting dN/dz for strong lines at $W \geq 0.32\text{\AA}$ are plotted in Fig. 11 as the heavy solid curve (CDM) or the heavy dotted curve (LCDM). The evolution is fitted best by $dN/dz = 75[(1+z)/4]^{2.5}$. This index is different from the γ found from τ_{HI} , which was 2.1, due to the evolution of the column density distribution in Fig. 9d, where high column densities are more common at large redshifts and have stronger saturation. We should, however, compare these counts with observations not polluted by the proximity effect. The data points with error bars are from Bechtold (1994). The shaded region is the fitting formula for the “old-subset” sample in Lu et al. (1991) (note that this sample is selected at $W \geq 0.36\text{\AA}$). Lines can be selected not only by the equivalent width, but also by the central minima of the line profiles if the profiles are resolved as in Keck HIRES data. The two thin curves in the figure are for lines with the minimum transmitted flux less than 0.5; the solid curve is for the CDM model and the dotted curve for the LCDM model. The best fit for this definition is $dN/dz \propto (1+z)^{1.5}$. There

are no data published yet for comparison with these curves.

5. Similarity between Simulations and Observations

5.1. A real synthetic sample

Let us compare directly the Keck spectrum of HS1700+64 and synthetic spectra in this section. The data were obtained by D. Tytler and are discussed in detail in Zheng et al. (1996). As we discussed before, the Gunn-Peterson opacity of HS1700+64, $\tau_{HI} = 0.22 \pm 0.01$, is greater than the global average value 0.153 at $z = 2.4$. Therefore we use $J_{21} = 0.1$ with $\Omega_b = 0.015h^{-2}$ to simulate absorption spectra for this specific quasar, which produces $\tau_{HI} = 0.21$ in both the dark matter models.

The Keck spectrum in the redshift range $z = 2.3$ to $z = 2.5$ is plotted in the upper panel in Fig. 12. A careful check reveals many line profiles are asymmetric or contain shallow non-Voigt wings (such as the ones at 4033Å, 4127Å, 4207Å and 4251Å), which reflect typically absorptions of asymmetric mass clumps in the diffuse IGM model. Particular groups of lines, such as those regions at 4070Å to 4077Å, 4139Å to 4143Å and 4216Å to 4222Å, would require a considerable number of weak lines to explain, but they can be easily produced by mass clusterings instead of individual discrete clouds.

A synthetic sample in the CDM model is plotted below the Keck data (the corresponding sample in the LCDM model is almost indistinguishable and thus has not been plotted). The Keck data were obtained at a resolution of 3 km s^{-1} , so we can simply neglect the line-spread-function in the simulation. Gaussian noise of zero mean and variance 0.04 has been added to each pixel in the simulated spectrum to match the observations. The similarity between the simulation and the real data is very good.

The simulation spectrum is analyzed using an accurate (but slow) spectral fitting program called “VPFIT” by R. F. Carswell et al.. In Table 2, we list all lines with positions, b parameters and column densities. Lines with $N_{HI} \leq 10^{12.5} \text{ cm}^{-2}$ are uncertain and are not included in the table. The vertical bars in Fig. 12 mark the position of the lines in the table. There are several differences between the original, intrinsic absorbers and the lines selected by “VPFIT”. 1) Some intrinsic absorbers have been blended together to form *one* strong line, e.g. three absorbers with total intrinsic column density $3 \times 10^{14} \text{ cm}^{-2}$ are blended to one strong feature at 4092Å that has the fit column density $\log N_{HI} = 17.0$. In real observations, one usually needs associated metal lines to fix the number of sub-components. 2) A few absorbers with broad density wings have to be fitted by *two* Voigt lines, one with a small b for the main part of the profile and the other with a large b for the absorption wing. The absorber with intrinsic $N_{HI} = 7.5 \times 10^{13}$ at 4058Å, for example, is split into two lines with a total $N_{HI} = 2.7 \times 10^{14}$. 3) Many weak features which can be marginally identified by eye in the synthetic spectrum are actually associated with small mass

clumps, not noise. This would suggest that similar features in the Keck data may be real too.

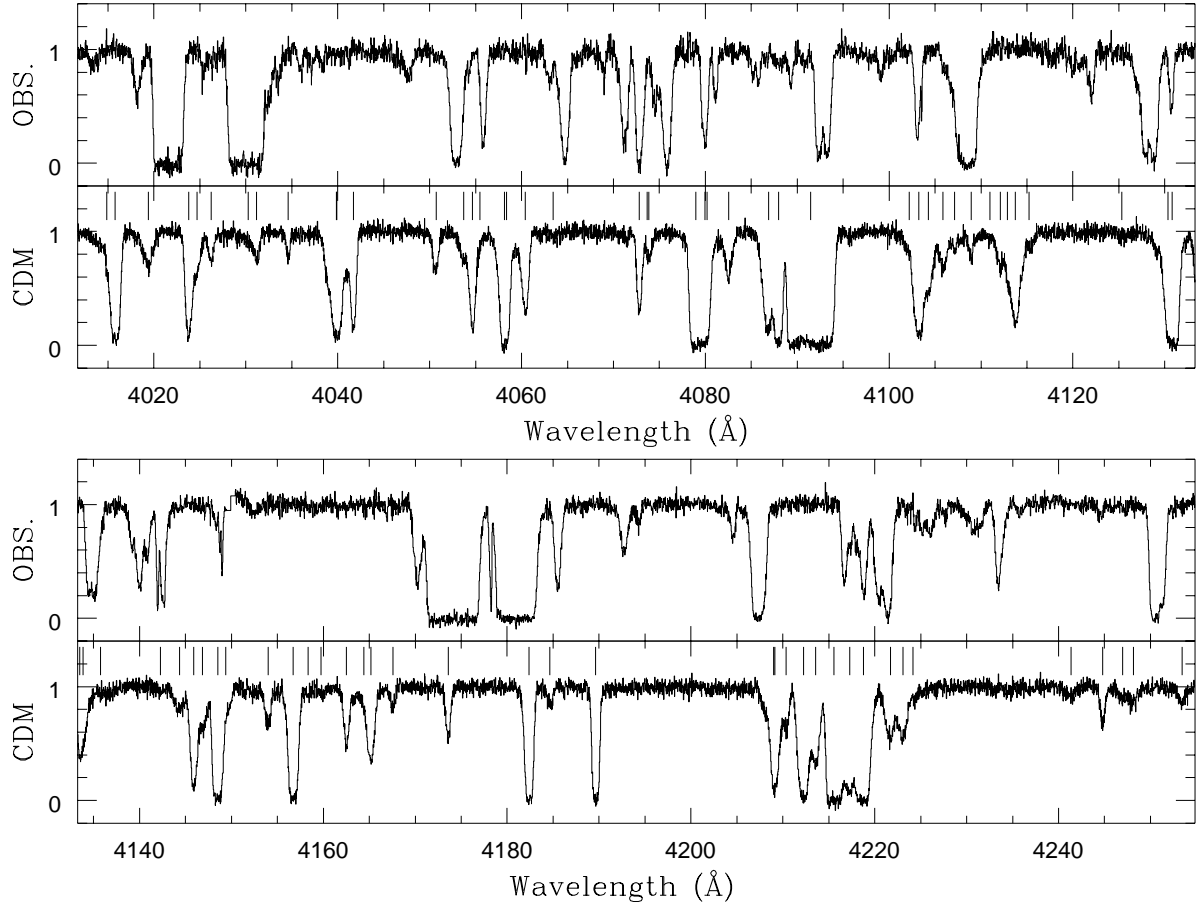


Fig. 12.— The Keck spectrum of HS1700+64 in the redshift range 2.3 to 2.5, and a simulated spectrum in the CDM model. All lines with Voigt-fit column densities exceeding $10^{12.5} \text{ cm}^{-2}$ are marked as vertical bars in the synthetic spectrum.

As a summary, the total number of lines with $\log N_{HI} \geq 12.5$ in Table 2 is 79, while the number of intrinsic clouds is 135 in the same column density range. So the intrinsic number is approximately 1.70 time greater than the number from the VPFIT software.

The histograms of the fitted b parameter are shown in Fig. 13 as the light histogram. The thick-line histogram is from the observation of Carswell (1989). The shape of the simulated distribution is quite consistent with the observation (see also Hunstead 1988; Press & Rybicki 1993). Both the distributions show that most of the lines have $b = 20$ to 40 km s^{-1} and that an extensive tail exists between 40 to 100 km s^{-1} .

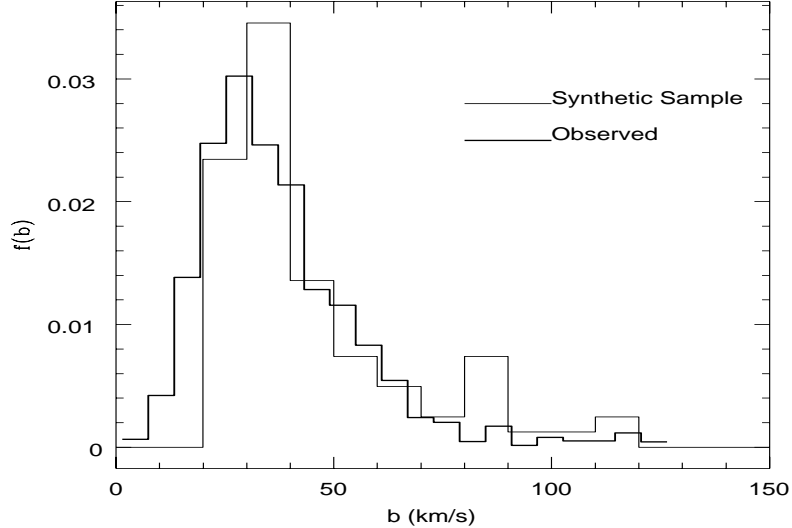


Fig. 13.— The probability distribution of the b parameters of the Voigt-fit Ly α lines in our simulated spectrum (Fig. 12 and Table 2) is shown as the light histogram. The heavy histogram is from observations (Carswell 1989).

5.2. Evolution of specific clouds

Consider the IGM distribution in the box of $5 h^{-1}\text{Mpc}$ around $z = 2.4$ in Fig. 12. The density ρ , peculiar velocity v and absorption spectrum are plotted in Fig. 14 for the same IGM mass distribution at three different redshifts : $z = 2, 3$, and 4 . The solid lines in the ρ panels are the normalized density distribution and the dashed lines the “maximal smoothed” reference field used in the line identification.

We trace specifically 6 intrinsic absorbers in the ρ panel at $z = 4$, which are marked as vertical bars. The absorbers are selected according to our selection procedure in §3.2. Their intrinsic column densities are listed in Table 3 as $\log N_{int}$. The vertical bars in the “Spectrum” panels mark the fit absorption lines which correspond to the intrinsic absorbers. The shifts of the line positions are due to the peculiar velocity. The dotted curves are the restored spectra from the fit lines. The fit column density $\log N_{fit}$ and b_{fit} parameters are also listed in Table 3. Note that the shape of the velocity profile around the strongest line, line 3, agrees well with the globally averaged velocity profile in Fig. 6. We see that mass is falling from the two sides toward the line center in comoving space.

At redshift 4, absorbers 1, 2 and 3 are seriously blended in both the ρ distribution and the spectrum, so it is not surprising that their fit column densities are different from the intrinsic values. Yet the sum of the intrinsic column densities, $10^{15.34} \text{ cm}^{-2}$, is comparable to the sum

of the fit column densities $10^{15.50}$. Absorbers 5 and 6 are relatively separated from the blended region, so their N_{int} are approximately equal to the fit N_{fit} .

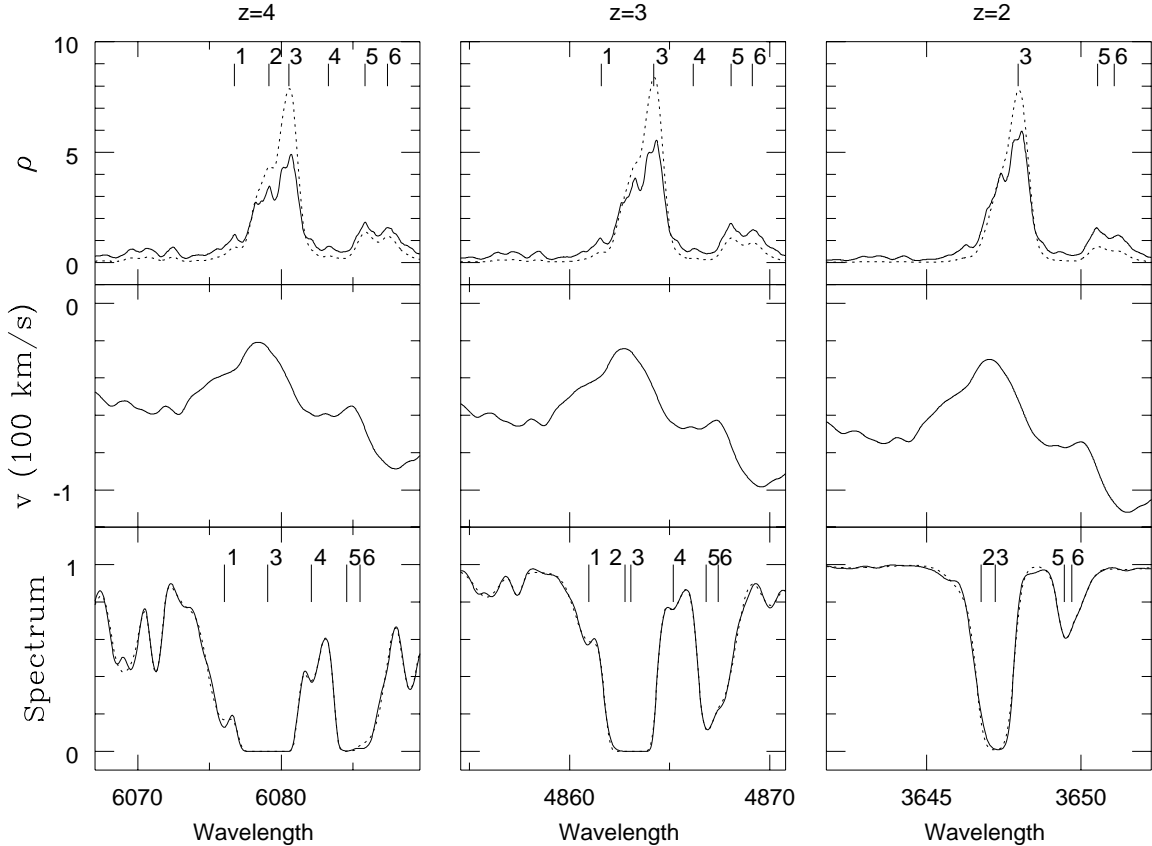


Fig. 14.— Evolution of the IGM in the comoving box $5h^{-1}\text{Mpc}$ around 4133\AA at $z = 2.4$ in Fig. 12 at three different redshifts, $z = 4$, $z = 3$ and $z = 2$. The upper panels show the density distribution (solid lines) and the “maximal smoothed” reference field (dashed lines) where six intrinsic absorbers are marked and discussed in the paper. The middle panels show the peculiar velocity. The lower panels are the absorption spectra. The marked numbers are lines from the Voigt-fit and the dashed curves are the restored spectra from these lines.

At $z = 3$ and $z = 2$, the density fluctuation grows. Overdense regions, such as absorber 3, are becoming even denser, and small density clumps, such as absorbers 1 and 4, are being destroyed or merged into large absorbers. Because the mean cosmological density is decreased, all the clouds have evolved to smaller column densities. Their b parameters are usually smaller at lower redshifts too. Of particular interest is the cloud marked Number 2. At $z = 4$, it has been selected by our “maximal smooth” identification. Because its absorption is very strong and blended with cloud 3, we only detect one spectral line (marked Number 3) from the two absorbers. At $z = 3$, cloud 2

can no longer be regarded as a separate cloud in the “maximal smooth” identification (although it is still present in the “no smooth” identification, of course); however, the asymmetric profile of the merged absorption does require another component in the Voigt fitting, which is marked as line 2. It is noticed that cloud 2 does not match line 2 in either position or column density. This shows that the Voigt profile fitting is not efficient in revealing intrinsic structures if the IGM is not in discrete clouds, but is continuously distributed in space as we suggested here.

We also notice that the three underdense clumps around 6070 Å at $z = 4$ are disappearing in the spectra from $z = 4$ to $z = 2$, which can be understood again by the two effects : their density contrasts become even lower due to clustering, and the average neutral hydrogen density is lower due to the expansion of the universe.

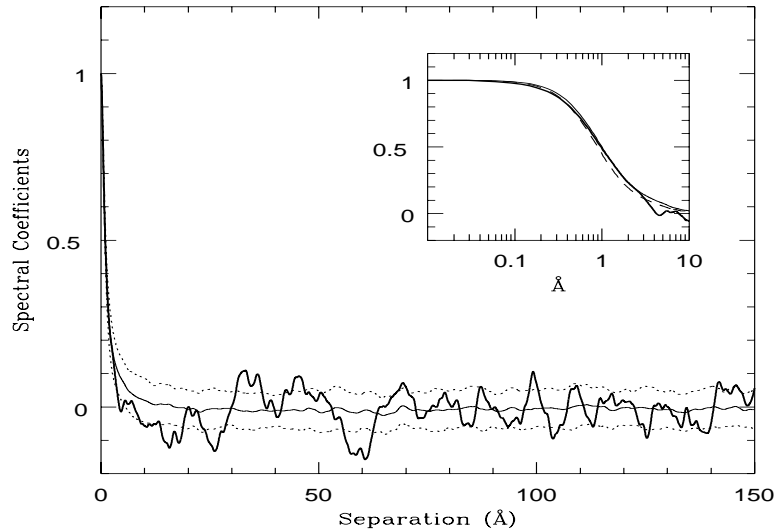


Fig. 15.— Averaged spectral coefficients vs. separations for 1000 synthetic samples similar to that in Fig. 12. The two dotted curves show the 1σ error bars in the simulations. The graph in the insert is the same plot but on very small separations where we have also plotted the LCDM model as the dashed curve. The heavy solid curve is from the Keck observation of HS 1700+64.

5.3. Autocorrelation coefficients

We can view an absorption spectrum as a time series. To see how the spectrum $f(k), k = 1, 2, \dots, N$, is correlated at the separation of l pixels, the following autocorrelation coefficients can be used (Bi 1993; MCOR) :

$$r_c(l) = \frac{1}{N\sigma^2} \sum_{k=1}^{N-l} [f(k) - \langle f \rangle][f(k+l) - \langle f \rangle], \quad l = 0, 1, 2, \dots, N-1; \quad (19)$$

where

$$\langle f \rangle = \frac{1}{N} \sum_{k=1}^N f(k), \quad \sigma^2 = \frac{1}{N} \sum_{k=1}^N (f(k) - \langle f \rangle)^2.$$

The cross-correlation coefficients between two parallel spectra can be defined in the same way.

Fig. 15 plots the mean coefficients vs. l (in units of Å) of 1000 synthetic samples simulated in the redshift box 2.2 to 2.6 in the same model as in Fig. 12. The graph in the insert is the same plot but at very small separations. The LCDM model differs from the CDM model in this figure only at small separation, so is shown as the dashed curved in the insert graph. The 1σ error bars in the CDM model are plotted as the two dotted curves. The heavy solid curve is from the Keck observation of HS 1700+64 in the same redshift range.

Significant correlations are found within 10Å (or $3.94 h^{-1}$ Mpc in comoving space in the CDM model), which should be basically attributed to individual Voigt profiles and density wings. The data and simulations match each other within the 2σ error bars. If the wing does not exist, i.e., clouds are all zero-sized, the coefficients will drop to zero at a smaller separation (see Fig. 8 of Bi 1993 and Fig. 13 of MCOR). Although the initial density distribution contains fluctuation powers on scales $> 10h^{-1}$ Mpc, no correlation can be found in the spectral coefficients on these large scales because the signals are too weak.

5.4. Spectral Filling Factor

A useful statistical quantity is the cumulative distribution of the transmitted flux (see MCOR), or *spectral filling factor*. The observational calculation of the Keck spectrum is shown as the heavy solid curve in Fig. 16. The light solid curve and the dotted curve are from synthetic spectra in the CDM and LCDM models, respectively. In order to mimic the observation best, the simulation samples were performed in the redshift interval 2.2 to 2.6; in each pixel independent Gaussian noise of zero mean and variance 0.04 has been added to match the noise in the Keck spectrum. The statistical 1σ error bars are so small that we may ignore them in the figure. Noise in the simulation gives a little bit more filling factor at large flux and a little bit less filling factor at small flux.

The filling factor of the CDM model agrees well with that observed except for a small difference ~ 0.027 at large fluxes. As we have pointed out early in the paper, the present IGM model contains very few or no Lyman limit systems or damped systems. But the real Keck spectrum does. Since these clouds have always absorbed flux to zero, adding them to the model will account for the difference to allowed error bars. The LCDM model has stronger clustering and thus slightly less low density clumps, or equivalently, less shallow spectral absorptions. The density fluctuation in this model is 1.25, compared to 1.18 in the CDM model. Both the models are successful in explaining the existence of very weak absorption features.

In an IGM with a very high variance, most of the mass would reside in discrete clumps (or

clouds) and most of the volume would be nearly empty as underdense regions are destroyed. Due also to the saturation of overdense clouds in the Ly α absorption, such a medium would require a lower UV background radiation to give the correct HI Gunn-Peterson opacity. (For the HeII GP opacity, the medium would require a very high population ratio.) This is the case for the old, “standard” cold-dark-matter (SCDM) model with $\Gamma = 0.5$, which has $\sigma = 2.52$ at $z = 2.4$. In order to get the correct effective opacity, we need to use $J_{21} = 0.005$, which is much too small to be consistent with the proximity effect. The strong clustering of the model will also produce a very different spectral filling factor function, as shown in Fig. 16.

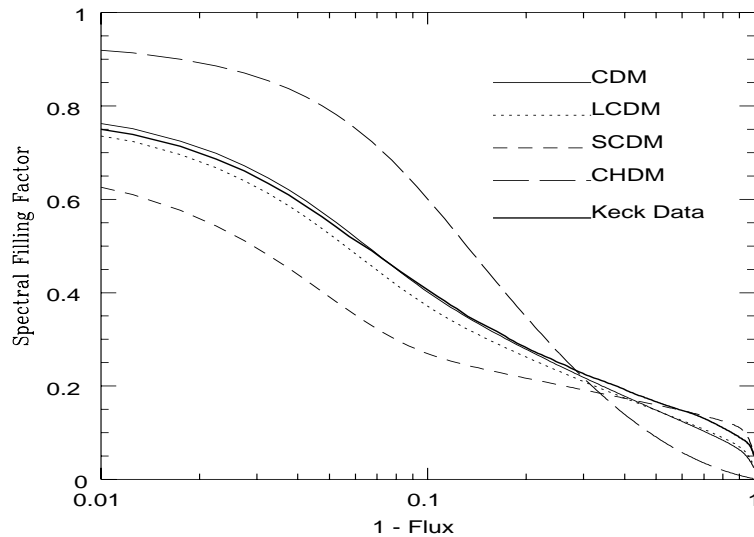


Fig. 16.— Spectral filling factor vs. the flux decrement in the CDM (solid line), LCDM (dot line), SCDM (dashed line) and CHDM (long dashed line) models. The heavy solid curve is from the Keck observation of HS 1700+64. The theoretical curves have all had noise added to approximate the noise in the data for HS 1700+64.

On the other hand, an IGM with too low a variance would have difficulty in making line-like features in the Ly α absorption because of insufficient density variations within clouds. Since more clouds are not saturated, we need a higher UV flux for the correct ionization and the effective opacity. However, the absorption would become severely blended even at low redshifts. For example, the cold-plus-hot dark-matter (CHDM) model with $\Omega_{hot} = 0.3, \Omega_{cold} = 0.7$ (e.g. Klypin et al. 1993) has $\sigma = 0.64$ at $z = 2$. We need $J_{21} = 0.16$ to get the correct effective opacity, but the absorption spectrum will look too blended to be acceptable in the simulations. We expect to see a different spectral filling factor function too.

The spectral filling factors in the SCDM and CHDM models are plotted as the dashed and long dashed curves in Fig. 16. Although we can change J_{21} to obtain the observed opacity, these model distributions in the figure are completely inconsistent with the observation. We thus

conclude that the $\Gamma = 0.3$ CDM model and the LCDM model are favored not only by other cosmological considerations but also by Ly α forest observations. The $\Gamma = 0.5$ SCDM model and the CHDM model fail in the test of the Ly α forest.

5.5. Comparisons with MCOR

Besides using real observations, we can compare our LCDM model with the same model in MCOR in order to check how it compares with hydrodynamical simulations. Some of the comparisons have already been discussed above (e.g Fig. 4c and Fig. 8). The spectral filling factor function provides another excellent comparison. Fig. 17 shows such filling factors at three redshifts $z = 2, 3$ and 4 in our LCDM model. Unlike Fig. 16, these curves have no added noise. Compared to MCOR's Fig. 11b, our curves predict slightly more pixels with fluxes close to 1 because of somewhat stronger mass clustering in our simulation.

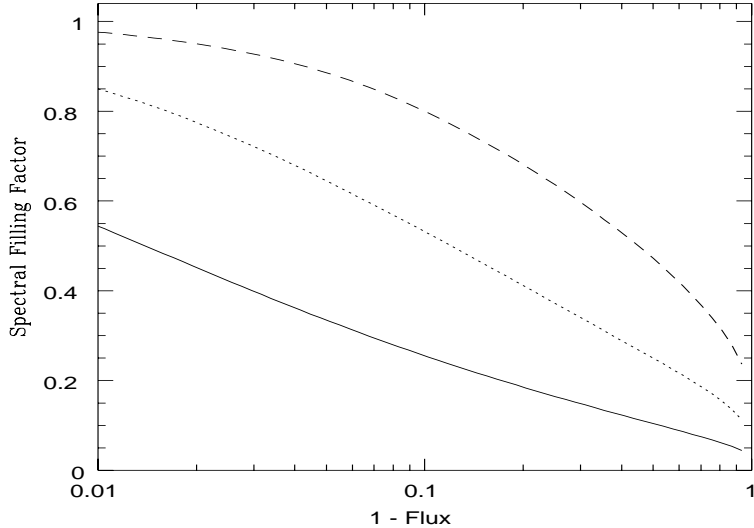


Fig. 17.— Spectral filling factor vs. the flux decrement in the LCDM model. The solid, dotted and dashed curves are for $z = 2, 3$ and 4 , respectively. These curves may be compared with similar ones given by MCOR's Figs. 11b.

Fig. 18 is a plot of the mass fraction coming from pixels that have transmitted flux smaller than a threshold value F (see Fig. 21 of MCOR). MCOR have a different procedure to simulate a spectrum, i.e. they first transform the density distribution into velocity space using the peculiar velocity and then calculate the absorption spectrum regardless of the peculiar velocity. Therefore, the mass fraction they derived in their Fig. 21 is in velocity space, instead of the original comoving space. In order to account for the difference, we use zero velocity in the calculation of Fig. 18.

Our plots agree with the corresponding plots of MCOR in general, although we are using a

quite different approach to the problem. There are two other factors that may bring uncertainties into the comparisons. First, MCOR did not use the Voigt profile, but used the pure thermal Gaussian profile in their spectral calculation. Second, the grid size in their simulation is $34h^{-1}\text{kpc}$ in comoving space, so their spectrum cannot be resolved below this limit ($4.4h^{-1}\text{ km s}^{-1}$ in velocity). Both of these factors can account for the small differences between the results of our calculations and theirs.

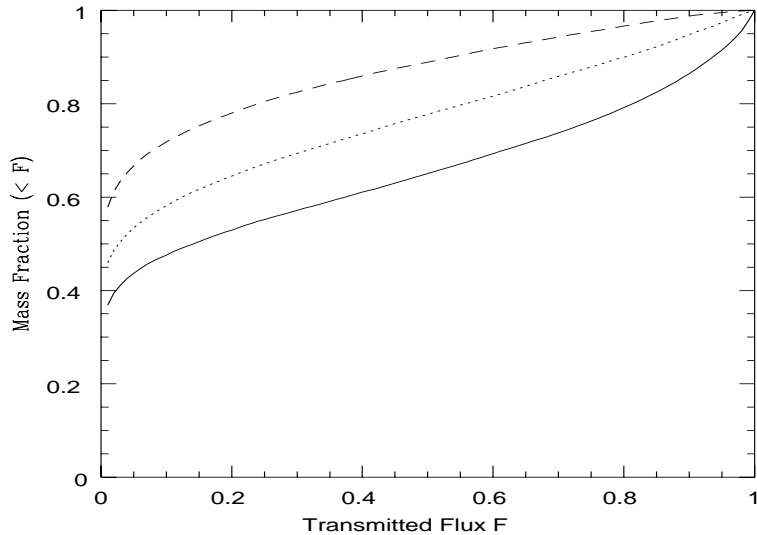


Fig. 18.— Mass coming from pixels with transmitted flux less than a given threshold at $z = 2$ (solid), 3 (dotted) and 4 (dashed) in the LCDM model. This figure may be compared with a similar one given by MCOR’s Fig. 21.

6. Summary

In this paper, we have argued that the intergalactic medium should be regarded as a continuous medium with density fluctuations that result from the growth of primordial dark matter fluctuations, as opposed to the conventional view of discrete clouds immersed in a smooth intercloud medium. With this paradigm shift, the long-held distinction between the Gunn-Peterson effect (arising from the diffuse intercloud medium) and the Bahcall-Salpeter effect or Ly α forest of discrete absorption lines (arising from denser clouds) no longer makes sense. The dividing line between these aspects of the IGM is arbitrary. If one were to use the universal mean baryon density to distinguish between “clouds” and the “intercloud medium”, for example, this would correspond to absorption features with an estimated column density of about $10^{13.5}\text{ cm}^{-2}$ at $z = 3$. Lower column density features typically come from regions that are below the mean density. At $z = 3$ our model indicates that about 30 percent of the mass, occupying 70 percent of space, would fall in this category. Most of the baryonic mass is in the moderately overdense

fluctuations that produce the well-studied Ly α forest.

We summarize our main conclusions further as follows.

1) The nature of the IGM at $z = 2$ to $z = 4$.

From both our analytical calculation and the hydrodynamic simulation of Cen et al. (1994) and MCOR, we conclude that the fluctuation variance of the density field of the IGM is close to unity in the redshift range ($z = 2 \rightarrow 4$) where most of the Ly α forest is observed. This is a special phase in the evolution of the IGM when both overdense and underdense clumps are significant in appearance. Mass is moving generally from low densities to high densities, but has not yet arrived at the final virialized stage when the clumps are stable in proper space. Dark matter fluctuations would act like magnets that attract the baryonic medium to their potential wells, but do not necessarily confine the baryons. Pressure confinement cannot be achieved. There are no distinguished thermal phases in the medium from which we can discriminate different thermal components. The whole medium appears as one diffuse and continuous fluid. This median fluctuation of the IGM is important in producing the correct HI opacity and the number of Ly α lines observed. The lognormal hypothesis appears to provide an excellent description of the density distribution of intergalactic gas in the non-linear regime at $z < 4$.

2) The structure within Ly α clouds.

In the diffuse IGM, our term “clouds” actually refers to all fluctuated density clumps which have either overdensity above the mean or underdensity below the mean. In fact, typical clouds and thus typical Ly α lines have just the mean mass density. For example, at redshift 3, clouds of column density $10^{11.5}$, $10^{13.5}$ and $10^{15.3}$ cm $^{-2}$ have mass density that is 0.1, 1 and 10 times the mean. The variation of (neutral) density within a cloud is best described by an exponential profile that peaks at the cloud center and declines outside the Jeans length. The origin of the density wing is actually due to the fluctuation nature of the IGM in which we cannot distinguish one cloud from another in space. However, the density wing has a very important implication : it broadens the absorption profile significantly. A wing of any absorber will resemble another cloud with a lower column density. For instance, a cloud with $N_{HI} = 10^{14.5}$ cm $^{-2}$ has the same neutral hydrogen distribution as an $10^{12.5}$ cm $^{-2}$ cloud at the comoving wing distance $0.8 h^{-1}$ Mpc, so it would have the detectable size $0.8 h^{-1}$ Mpc.

The peculiar velocity causes mass to fall toward the cloud center where the dark matter potential is minimized in comoving space. However, all clouds below 10^{16} cm $^{-2}$ are still expanding in proper space, because the peculiar velocity is not large enough to overcome the Hubble velocity. For clouds above $10^{13.5}$ cm $^{-2}$, the velocity is comparable to the thermal b parameter, so the resulting profile will be narrower. This effect is just opposite to the density wing. For an individual cloud, the velocity could appear as turbulent motions because it is not necessarily symmetric.

One effect that has been neglected in the present study is shock waves in the central regions of high column density absorbers, which can be anticipated in the simple Zel'dovich approximation

and have actually been observed in hydrodynamical simulations (e.g. Cen et al. 1994). Two mass streams from opposite directions along the principal axis are falling toward the center of a pancake. If thermal pressure cannot overcome the motions, they will impact each other and leave a cooling mass layer at the cloud center. Such a cooling layer will produce extra neutral hydrogen and thus will enhance the Ly α absorption opacity. However, a statistical histogram of density vs. temperature in the simulation of MCOR showed this is important only for clouds with $N_{HI} \geq 10^{15}$ cm $^{-2}$. Most of Ly α forest cloud discussed in this paper will not be affected by such shock waves.

3) The number density of clouds.

The total number of all clumps in the IGM is determined by the number of dark matter potential wells when smoothed on the Jeans scale. Since the Jeans length is roughly a constant in comoving space, the “global” number will be more or less fixed. The same cloud with a high column density will evolve to lower and lower column densities at later times because the proper density is decreasing. The column density distribution function at one redshift can be identified with that at a lower redshift by shifting the column density by a constant decreasing factor. Thus we expect to have more low column density absorbers at $z = 2$ than at $z = 4$.

Our simulation is based on the assumption that the UV background intensity is constant between $z = 4$ and $z = 2$, yet the effective opacity and the number counts of Ly α lines are quite consistent with those observed. Therefore we do not need to introduce any evolution of the UV background in that range.

4) The baryonic density

For both the CDM and LCDM models considered here, matching the observed effective opacity in the Ly α forest requires an appropriate choice of Ω_b^2/J_{21} . If we assume $\Omega_b = 0.015h^{-2}$, a nominal value consistent with standard Big Bang nucleosynthesis, then both models require $J_{21} \simeq 0.2$, somewhat lower than the value estimated for quasars at $z = 2 - 3$, and substantially lower than the estimate that $J_{21} = 1.0_{-0.3}^{+0.5}$ from the proximity effect (Cooke et al. 1996). Alternatively, if we adopt $J_{21} = 0.5$ as estimated by Haardt & Madau (1996), then we require $\Omega_b = 0.025h^{-2}$. This is at the high end of the range of values consistent with standard Big Bang nucleosynthesis. It is, however, compatible with the value found recently by Tytler, Fan & Burles (1996) from a measurement of a low deuterium abundance at high redshift. Our results are obviously incompatible with the much lower value of Ω_b deduced by Rutgers & Hogan (1996) from a measurement of a high deuterium abundance.

5) Statistics of absorption spectra

We have compared the Ly- α forest of HS 1700+64 with synthetic samples in the CDM and LCDM models using several statistical quantities which depend sensitively on spectral shapes. The b parameter describes the temperature or the width of an individual line profile. The spectral filling factor represents the percentage of pixels with flux below a given limit. It is a useful quantity that can be measured in observations. A strong clustering in the IGM would result

in too small a filling factor to be accepted. The spectral autocorrelation coefficient reveals the correlation between flux at chosen separations. The most useful coefficients are within 10Å and are dominated by the Voigt profile and density wing.

6) Related studies.

While our model could still be modified somewhat in detail, the global picture and physical explanation of the IGM and the Ly α forest should be well described in the present calculation. There are several interesting subjects in the IGM models.

First, highly resolved Keck spectra would allow us to study small scale structures in the IGM, and to discriminate different cosmological parameters. Beside the traditional Voigt fitting, statistics like the spectral filling factor and the autocorrelation function would be easy to compute and even more clear in revealing other important absorption features, especially weak features. The Ly α forest is very useful in model diagnostic checking. For example, if the standard deviation σ of the IGM is changed by a factor of 2, such as in the $\Gamma = 0.5$ CDM model and the cold-plus-hot dark matter model, the resulting absorption spectra are already inconsistent with observations and the models can probably be ruled out.

Second, the present IGM model is able to explain the recent observations of the HeII Gunn-Peterson effect with a reasonable HeII to HI population ratio of 100 - 150. We will discuss this in detail in another paper (Davidson et al. 1996). The HeII absorption depends not only on the column density of a cloud but also on the cloud geometry because of different saturation in the curve-of-growth. The more extended the cloud is in space, the less saturation the absorption has. In the conventional Ly α cloud picture, a cloud with 10^{13} cm $^{-2}$ column density is already saturated in the HeII absorption. In the present model, because of extended spatial structures, most of such clouds still appear linear and thus make a dominant contribution in the HeII opacity.

Finally, we note that if the Ly α forest originates from continuous density variation in the IGM, one can in principle deconvolve the density field inversely from the forest. This will allow us to obtain very fine structures ($\sim 0.05h^{-1}$ Mpc) as well as large scale structures of the cosmic baryonic distribution at high redshifts for the first time.

We thank J.R. Bond, B. Espey, G. Kriss, J. Miralda-Escudé, C. Norman, J. Peebles, Y. Pei, J. Ostriker, D. Weinberg and W. Zheng for many stimulating discussions and suggestions. HGB is especially grateful to W. Zheng for his help in using the Voigt fitting software “VPFIT”. We thank D. Tytler for generously providing the Keck spectrum of HS1700+64. This work has been supported by NASA contract NAS 5-27000 to the Johns Hopkins University.

N_{HI}	$\log M/M_{\odot}, CDM$			$\log M/M_{\odot}, LCDM$		
	$z = 2$	$z = 3$	$z = 4$	$z = 2$	$z = 3$	$z = 4$
10^{16} cm^{-2}	12.2	11.6	11.2	12.3	11.8	11.4
10^{15} cm^{-2}	11.3	10.9	10.5	11.5	11.0	10.7
10^{14} cm^{-2}	10.7	10.2	9.8	10.8	10.4	9.9
10^{13} cm^{-2}	10.0	9.5	8.9	10.2	9.6	9.1
10^{12} cm^{-2}	9.3	8.6	8.1	9.5	8.8	8.3
Jeans Mass	10.2	9.9	9.7	10.5	10.2	9.9

Table 1: Baryonic Mass Associated with Typical Features in the Ly α Forest

Line	$z = 4$			$z = 3$			$z = 2$		
	$\log N_{int}$	$\log N_{fit}$	b_{fit}	$\log N_{int}$	$\log N_{fit}$	b_{fit}	$\log N_{int}$	$\log N_{fit}$	b_{fit}
1	14.05	14.16	62.6	13.39	13.54	55.0		see ³	
2	14.83		see ¹	see ²	13.69	272.0	see ²	13.44	77.8
3	15.14	15.49	55.5	14.91	15.07	46.5	14.34	14.35	36.4
4	13.57	13.67	38.6	12.92	12.94	30.0		see ³	
5	14.35	14.31	26.1	13.85	13.59	23.0	13.17	12.76	19.1
6	14.33	14.51	77.3	13.76	13.99	55.6	12.92	13.30	44.5

Table 3: Parameters of specific Ly α lines at different redshifts (intrinsic absorbers are selected according to the “maximal smooth” identification)

¹Because of blending and saturation, the line cannot be found by Voigt fitting in the spectrum.

²Selected only in the “no smooth” identification. The blended asymmetric absorption profile requires line 2 in the Voigt fitting, which, however, is not cloud 2.

³The intrinsic absorber is merged into absorber 3. In the Voigt fitting, the line is not required either.

REFERENCES

Bagla, J.S., & Padmanabhan, T. 1994, MNRAS, 266, 227

Bahcall, J.N., & Salpeter, E.E. 1965, ApJ 142, 1677

Bajtlik, S., Duncan, R.C., & Ostriker, J.P. 1988, ApJ, 327, 570

Bechtold, J. 1994, ApJS, 91, 1

Bechtold, J., Crotts, P.S., Duncan, R.C., & Fang Y. 1994, ApJ, 437, L83

Bi, H.G. 1993, ApJ, 405, 479

Bi, H.G., Börner, G., & Chu, Y. 1992, A&A, 266, 1

Bi, H.G., Ge, J., & Fang, L.Z. 1995, ApJ, 452, 90

Black, J.H. 1981, MNRAS, 1981, 197, 553

Blades, J.C., Turnshek, D.A., & Norman, C.A. 1988, *QSO Absorption Lines : Probing the Universe* (Cambridge: Cambridge University Press)

Bond, J.R., Kofman L., & Pogosyan, D. 1996, Nature, 380, 603

Bond, J.R., Szalay, A.S., & Silk, J. 1988, ApJ, 324, 627

Brainerd, T.G., Scherrer, R.J., & Villumsen, J.V. 1993, ApJ, 418, 570

Carlberg, R.G., & Couchman, H.M.P 1989, 340, 47

Carswell, R.F. 1989, in *The Epoch of Galaxy Formation*, ed. C.S.Frenk, R.S.Ellis, T.Shanks, A.F.Heavens, & J.A.Peacock (Dordrecht: Kluwer), 89

Cen, R., Miralda-Escudé, J., Ostriker, J.P., & Rauch, M. 1994, ApJ, 437, L9

Charlton, J.C., Anninos, P., Zhang, Y., & Norman M. 1996, Astro-ph Preprint 9601152.

Coles, P., & Jones, B. 1991, MNRAS, 248, 1

Cooke, A.J., Espey, B., & Carswell, B. 1996, to be published in MNRAS

Davidsen, A.F. 1993, Science, 259, 327

Davidsen, A.F., & Fountain, G.H. 1985, Johns Hopkins APL Technical Digest, 6, 28

Davidsen, A.F., Kriss, G.A., & Zheng, W. 1996, Nature, 380, 47 (DKZ)

Davidsen, A.F., Kriss, G.A., Zheng, W., & Bi, H.G. 1996, in preparation

Dinshaw, N., Impey, C.D., Foltz, C.B., Weymann, R.J., & Chaffee, F.M., 1994, ApJ, 437, L87

Dobrzycki, A., & Bechtold, J. 1996, ApJ, 457, 102

Efstathiou, G., Bond, J.R., & White, S.D.M. 1992, MNRAS, 258, 1p

Fang, L.Z., Bi, H.G., Xiang, S.P., & Börner, G. 1993, ApJ, 413, 477

Gunn, J.E., & Peterson, B.A. 1965, ApJ 142, 1633

Haardt, F., & Madau, P. 1996, ApJ, 461, 20

Hernquist, L., Katz, N., Weinberg, D.H., & Miralda-Escudé, J. 1996, ApJ, 457, L51

Hu, E.M., Kim, T., Cowie, L.L., Songaila, A., & Rauch, M. 1995, AJ, 110, 1576

Hunstead, R.W. 1988, in *QSO Absorption Lines : Probing the Universe*, ed. J. Blades, D. Turnshek, & C. Norman (Cambridge : Cambridge University Press), 71

Jakobsen, P., Boksenberg, A., DeHarveng, J.M., Greenfield, P., Jedrzejewski, R., & Paresce, F. 1994, Nature, 370, 35

Jenkins, E.B., & Ostriker, J.P. 1991, ApJ, 376, 33

Klypin, A., Holtzman, J., Primack, J. R., & Regos, E. 1993, ApJ, 416, 1

Lynds, C.R. 1971, ApJ, 164, L73

Lu, L.M., Wolfe, A.M., & Turnshek, D.A., 1991, ApJ, 301, 522

McGill, C. 1990, MNRAS, 349, 429

Miralda-Escudé, J. 1993, MNRAS, 262, 273

Miralda-Escudé, J., & Ostriker, J.P. 1990, ApJ, 350, 1

Miralda-Escudé, J., & Rees, M.J. 1993, MNRAS, 260, 624

Miralda-Escudé, J., Cen, R., Ostriker, J., & Rauch, M. 1996, ApJ, in press (MCOR)

Oort, J.M. 1981, A&A, 94, 359

Ostriker, J.P., & Ikeuchi, S. 1983, ApJ, 268, L63

Petitjean, P., Webb, J.K., Rauch, M., Carswell, R.F., & Lanzetta, K. 1993, MNRAS, 262

Peebles, P.J.E. 1974, ApJ, 392, 15

Peebles, P.J.E. 1980, *The Large Scale Structure of the Universe* (Princeton: Princeton Univ. Press)

Peebles, P.J.E. 1993, *Principles of Physical Cosmology* (Princeton: Princeton Univ. Press)

Press, W.H., & Rybicki, G.B. 1993, ApJ, 418, 585

Rees, M.J. 1986, MNRAS, 218, 25p

Rugers, M., & Hogan, C.J. 1996, preprint astro-ph 9603084

Sarazin, C.L., & Bahcall, J.N. 1977, ApJS, 34, 451

Sargent, W.L. W., Young, P.J., Boksenberg, A., & Tytler, D. 1980, ApJS, 42, 42

Tytler, D. 1995, private communication

Tytler, D., et al. 1995, in *QSO Absorption Lines* eds. Bergeron, G., Mevian, G. & Wampler, J., p289

Tytler, D., Fan, X., & Burles, S. 1996, Nature, 381, 207

Walker, T.P., Steigman, G., Schramm, D.N., Olive, K.A., & Kang, H.S. 1991, ApJ, 376, 51

Weymann, R.J., Carswell, R.F., & Smith, M.G. 1981, ARAA, 19, 41
Wright, E.L., et al. 1994, ApJ, 420, 450
Zhang, Y., Anninos, P., & Norman, M.L. 1995, ApJ, 453, L57
Zheng, W., & Davidsen, A.F. 1995, ApJ, 440, L53
Zheng, W., et al. 1996, in preparation

TABLE 2
PARAMETERS OF LY α FOREST LINES

Wavelength	$\log N_{HI}$	σ_N	b	σ_b	Wavelength	$\log N_{HI}$	σ_N	b	σ_b
4014.87	13.41	0.03	93.18	4.02	4015.79	14.22	0.01	35.65	0.47
4019.38	13.40	0.01	57.75	1.09	4023.81	13.95	0.01	29.38	0.29
4024.71	13.31	0.01	34.11	1.02	4026.24	13.13	0.01	35.14	1.02
4030.25	12.97	0.05	87.82	8.24	4031.17	12.99	0.03	26.71	1.46
4034.62	12.88	0.01	23.44	0.54	4039.84	14.14	0.01	74.38	0.65
4039.91	13.76	0.02	30.61	0.84	4041.70	13.78	0.00	23.86	0.16
4050.70	13.23	0.00	31.19	0.43	4053.69	13.24	0.01	45.72	0.93
4054.67	13.81	0.00	26.35	0.26	4055.48	12.69	0.03	26.33	2.13
4058.16	14.37	0.01	30.54	0.34	4058.36	13.61	0.01	114.64	4.71
4060.42	13.68	0.00	31.10	0.30	4063.43	12.53	0.04	81.76	9.94
4072.82	13.57	0.00	22.56	0.15	4073.87	12.69	0.03	22.91	0.98
4073.67	13.05	0.02	81.91	2.40	4078.95	14.80	0.01	31.40	0.16
4079.98	14.24	0.00	34.71	0.13	4080.20	13.51	0.00	188.66	2.33
4082.55	13.29	0.00	35.52	0.27	4086.87	14.07	0.00	47.18	0.50
4087.97	14.43	0.02	24.44	0.37	4091.45	see ^a			
4102.19	13.17	0.05	66.49	4.82	4103.21	14.11	0.01	36.86	0.37
4104.27	13.66	0.00	46.29	0.54	4105.85	13.28	0.01	34.90	0.56
4107.12	13.01	0.01	53.33	1.84	4108.95	13.02	0.01	32.36	0.71
4110.97	12.67	0.03	60.07	4.63	4112.09	13.22	0.02	32.41	1.08
4112.88	13.16	0.05	26.28	1.73	4113.76	13.94	0.01	43.92	0.80
4115.22	13.00	0.02	50.16	2.39	4125.31	12.63	0.03	59.76	5.36
4130.37	13.71	0.01	109.03	1.54	4130.81	14.67	0.01	37.46	0.36
4133.49	13.11	0.04	20.76	1.00	4133.85	13.59	0.01	46.58	0.86
4135.78	12.78	0.34	79.37	42.58	4142.27	12.58	0.01	55.09	2.28
4144.35	13.24	0.00	57.29	0.72	4145.89	13.89	0.00	28.14	0.10
4146.86	13.45	0.00	45.90	0.47	4148.51	14.47	0.01	30.55	0.16
4149.39	13.17	0.02	41.89	1.29	4153.98	13.25	0.01	34.91	0.67
4156.71	14.30	0.01	34.94	0.23	4158.37	12.53	0.03	32.42	2.97
4159.77	12.57	0.03	38.96	3.34	4162.53	13.43	0.01	31.12	0.45
4164.41	13.19	0.03	83.82	4.06	4165.20	13.64	0.01	32.64	0.55
4167.57	12.85	0.01	24.28	0.88	4173.58	13.28	0.00	23.40	0.24
4182.38	14.29	0.01	28.63	0.15	4184.66	12.85	0.01	26.13	0.66
4189.64	14.23	0.01	23.21	0.13	4209.01	13.69	0.02	89.01	1.57
4209.14	13.91	0.01	30.49	0.44	4210.37	13.11	0.03	23.39	0.95
4212.25	14.31	0.00	38.53	0.29	4213.56	13.74	0.00	36.39	0.42
4215.57	15.44	0.04	30.04	0.35	4217.28	14.55	0.00	116.99	0.68
4218.76	14.57	0.02	36.15	0.48	4221.71	13.59	0.00	49.40	0.51
4223.07	13.48	0.01	40.92	0.54	4224.14	12.96	0.03	85.79	5.26
4241.34	12.79	0.01	45.58	0.89	4244.82	13.08	0.00	25.11	0.22
4246.99	12.95	0.02	61.30	2.55	4248.17	12.87	0.03	40.27	1.35
4253.44	12.86	0.01	36.43	0.71					

^aassociated metal lines and Lyman limit system to fix the sub-components. If fitted by a single line, we find $N_{HI} = 10^{17.7} \text{ cm}^{-2}$.